

## A coupled THM-SPH computational framework for frozen soils and its applications for thawing-induced slope failure

Yanlian Lian<sup>a</sup>, Ha H. Bui<sup>a,\*</sup>, Giang D. Nguyen<sup>b</sup>

<sup>a</sup> Department of Civil and Environmental Engineering, Monash University, Australia

<sup>b</sup> School of Civil, Environmental & Mining Engineering, University of Adelaide, Australia

### ARTICLE INFO

#### Keywords:

Frozen soils  
Coupled THM modelling  
SPH  
Thawing-induced slope failure  
Active layer sliding permafrost

### ABSTRACT

Thawing-triggered slope failures and landslides are becoming an increasing concern in cold regions due to the ongoing climate change. Predicting and understanding the behaviour of frozen soils under these changing conditions is therefore critical and has led to a growing interest in the research community. To address this challenge, we present the first mesh-free smoothed particle hydrodynamics (SPH) computational framework designed to handle the multi-phase and multi-physic coupled thermo-hydro-mechanical (THM) process in frozen soils, namely the THM-SPH computational framework. The frozen soil is considered a tri-phase mixture (i.e., soil, water and ice), whose governing equations are then established based on  $u - p - T$  formulations. A critical-state elasto-plastic Clay and Sand Model for Frozen soils (CASM-F), formulated in terms of solid-phase stress, is then introduced to describe the transition response and large deformation behaviour of frozen soils due to thawing action for the first time. Several numerical verifications and demonstrations highlight the usefulness of this advanced THM-SPH computational framework in addressing challenging problems involving thawing-induced large deformation and failures of slopes. The results indicate that our proposed single-layer, fully coupled THM-SPH model can predict the entire failure process of thawing-induced landslides, from the initiation to post-failure responses, capturing the complex interaction among multiple coupled phases. This represents a significant advancement in the numerical modelling of frozen soils and their thawing-induced failure mechanisms in cold regions.

### 1. Introduction

Thawing-induced slope collapse and or cryogenic landslides [1] are commonly reported in permafrost and seasonally freezing regions. As temperatures rise, ice undergoes a phase change to water, releasing moisture that contributes to high pore-water pressure, decreases the shear strength of soil, and triggers the sliding failure of the slope. These landslides can further impact the local landscape and ecosystem [2,3] and threaten the infrastructure, including roads, pipelines and other earthworks [4]. Typically, there are two primary forms of cryogenic landslide: active layer sliding and retrogressive thaw slumps [1–3]. Active layer sliding involves an active layer of cohesive material sliding over the water-saturated boundary between the thawed layer and the permafrost, where the shear strength is decreased by high pore water pressure due to the melted ice. Retrogressive thaw slumps usually occur in ice-rich permafrost, particularly on steep slopes [1]. Over the past century, these landslides have accelerated because of global warming and climate

\* Corresponding author.

E-mail address: [ha.bui@monash.edu](mailto:ha.bui@monash.edu) (H.H. Bui).

change. Given the escalating threats, various fields, such as civil engineering and geotechnical engineering, have witnessed a rise in concern in recent years. As such, gaining an in-depth understanding of the mechanisms and predicting these failure behaviours has become increasingly crucial. Therefore, developing a comprehensive numerical tool for predicting thaw-induced landslides is essential.

The lack of such a comprehensive numerical tool can be attributed to several challenges, primarily the lack of a suitable constitutive model describing the complex behaviour of frozen soil and a numerical tool capable of handling the complicated THM process, including the large-deformation and post-failure responses. Frozen soil is a multi-phase material consisting of solid grains, ice, and water, whose mechanical behaviour is thus highly sensitive to temperature and confining stress [5]. This complexity has posed significant challenges to fully understanding frozen soil mechanics. Over the past decades, experimental studies have revealed various interesting phenomena of frozen soil, including frost heave, thaw settlement, pre-melting, creep and freezing-thawing cyclic effect [6–8]. While these findings have greatly contributed to the development of the constitutive model, a comprehensive understanding has not yet been achieved. Nevertheless, several constitutive models for frozen soil based on different constitutive stress concepts have been proposed, which can capture several essential characteristics of frozen soils [4,9–13]. In addition, incorporating these constitutive models, numerical tools, such as Finite Element Methods (FEM), have been employed to model boundary value problems, such as freezing heave or thawing settlement [4,11–14]. However, most of these applications are limited to small-deformation problems due to the challenge of mesh distortion issues [15–18]. Recent progress has been made in developing THM frameworks using the material point method (MPM) to address large deformation problems in geomaterials [19–21]. However, achieving a fully coupled THM framework remains challenging, as many adopted constitutive models are still decoupled from hydraulic and thermal processes [19, 21]. In particular, most constitutive models rely on simple elasto-plastic Mohr-Coulomb formulations for unfrozen soil, without accounting for temperature effects or phase change. Although Yu et al. [20] introduced an ice-dependent constitutive relationship, several critical features, such as phase-change-induced volume changes and coupled thermal-hydraulic-mechanical interactions, were not fully captured. More importantly, among existing studies, the evolution of the hydraulic field during phase change in cryogenic landslide simulations was not presented. Therefore, a comprehensive numerical framework capable of modelling thawing-induced slope failure, incorporating advanced constitutive models and large deformation, is still urgently required.

Smoothed Particle Hydrodynamics (SPH) is the eldest truly continuum-based mesh-free method, initially developed for astrophysical applications [22,23]. Since its early applications in solving large deformation of elastoplastic materials [24,25], SPH has been widely used to solve a range of challenging geotechnical problems, including granular flows [26–29], slope failures [30–35], soil-structure interactions [36–38], desiccation cracking in soils [39,40] and rock fractures [41–45], to name a few. Besides, fully coupled fluid-solid interaction problems have also been developed, using either the multi-layer [25,46–48] or the single-layer approach [15,16,18,49–57], covering the small-deformation consolidation problems and coupled flow-deformation and failure problems. However, despite several existing attempts to model THM processes using SPH, none of the existing studies have yet presented a fully coupled THM model capable of handling frozen soils.

This paper aims to address the aforementioned challenges by developing a fully coupled THM-SPH computational framework for modelling the large deformation and failure behaviour of frozen soil. The paper is organised as follows: First, governing equations for the tri-phase frozen soil mixture based on  $\mathbf{u} - p - T$  ( $\mathbf{u}$  stands for displacement,  $p$  denotes pore pressure and  $T$  is temperature) formulations are established. An advanced constitutive model, namely CASM-F, is then introduced to capture the essential behaviour of frozen soil subjected to the coupled THM process. Subsequently, the fully coupled THM governing equations are solved for the first time by a stabilised SPH computational framework implemented in our in-house code. The proposed method is verified through several benchmark problems, including heat conduction, coupled thermal-hydraulic (TH) and fully coupled THM applications. The model's capability is further demonstrated by simulating a one-dimensional freezing test. Finally, the framework is applied to a thawing-induced slope, illustrating its potential for fully coupled heat-flow and large deformation analysis in frozen soils.

## 2. Multi-phase frozen soil framework

Saturated frozen soil is a complex porous medium composed of multiple phases. To establish governing equations that effectively describe its behaviour, certain assumptions are necessary to make the mathematical formulations and numerical analysis tractable. In the present framework, the following assumptions are adopted for modelling frozen soils [12,58]:

- a. No mass exchange between water and soil, and between ice and soil.
- b. Crystal ice and solid grain are assumed to be incompressible.
- c. Terzaghi's effective stress concept is accepted.
- d. The Clausius-Clapeyron equation is accepted for thermodynamic equilibrium.
- e. The soil-water retention curve (SWRC) is accepted in the ice-suction relation.

It is worth noting that, while some of the above assumptions are adopted primarily for mathematical simplification, others reflect key physical characteristics of frozen soils. For example, assumption (b) is justified by the high bulk modulus of critical ice (i.e., 8–9 GPa), which makes its volumetric deformation negligible under typical engineering loading conditions. This allows ice to be treated as part of the solid skeleton, supporting assumption (c), where only unfrozen water contributes to pore-pressure, similar to conventional saturated soil models. Furthermore, assumption (e) is supported by the analogy between unsaturated and frozen soils: matrix suction arises from the water-air interface, while cryogenic suction arises from the water-ice interface. This analogy allows the SWRC to be considered applicable for describing ice-suction relationships in frozen soils [4]. With these assumptions, the computational

framework for frozen soil is derived from the principles of mass, momentum, and energy conservation. The Clausius-Clapeyron equation and SWRC are incorporated to model thermodynamic equilibrium and the temperature-ice-water interactions.

### 2.1. Definition of the partial density of the frozen porous medium

The representative volume element (RVE) of the saturated frozen porous medium is shown in Fig. 1. The pore void within the medium is assumed to be filled by water and ice. The partial density of each phase can be defined as:

$$\bar{\rho}_\alpha := n_\alpha \rho_\alpha, \text{ with } n_s + n_i + n_l = 1 \quad (1)$$

where the letter  $\alpha$  denotes the phase component, with  $s, i$ , and  $l$  being soil, ice and liquid phase, respectively;  $\rho_\alpha$  stands for the intrinsic mass density of each component; and  $n_\alpha$  is the void fraction for each phase, which can be written as follows:

$$n_s = 1 - n, \quad n_l = n S_r, \quad n_i = n S_i \quad (2)$$

where  $S_r$  denotes the degree of saturation of liquid water while  $S_i$  refers to ice phase. For saturated frozen soil, the following relation holds:

$$S_r + S_i = 1 \quad (3)$$

Accordingly, the total density is given by the summation of the partial density of each phase as follows:

$$\rho = n S_r \rho_l + n S_i \rho_i + (1 - n) \rho_s \quad (4)$$

Similar to the density, the partial stress of each phase can be defined as:

$$\begin{aligned} \bar{\sigma}_s &= (1 - n) \sigma_s \\ \bar{\sigma}_l &= -n S_r p_l \mathbf{I} \\ \bar{\sigma}_i &= -n S_i p_i \mathbf{I} \end{aligned} \quad (5)$$

where  $\bar{\sigma}_\alpha$  is the partial stress of phase  $\alpha$ ;  $\sigma_s$  is the stress on the soil skeleton; while  $p_l$  and  $p_i$  denote the pore water pressure and pore ice pressure, respectively. Using these basic concepts, the governing equations for the frozen soil based on  $\mathbf{u} - p - T$  formulations are derived in the next section.

### 2.2. Coupled THM governing equations

#### 2.2.1. Momentum balance equations

Similar to the computational framework for unsaturated soil developed in the authors' previous work [18,49,59], the behaviour of frozen porous media is governed by the interaction between each phase in the mixture. The mixture herein is considered a homogenised continuum that follows its governing equation. Based on this consideration, a general form of the linear momentum equation of each homogenised phase can be written as follows:

$$\bar{\rho}_\alpha \frac{d^a \mathbf{v}_\alpha}{dt} = \nabla \cdot \bar{\sigma}_\alpha + \bar{\rho}_\alpha \mathbf{b} - \sum_\beta \mathbf{R}^{\beta\alpha} \quad (6)$$

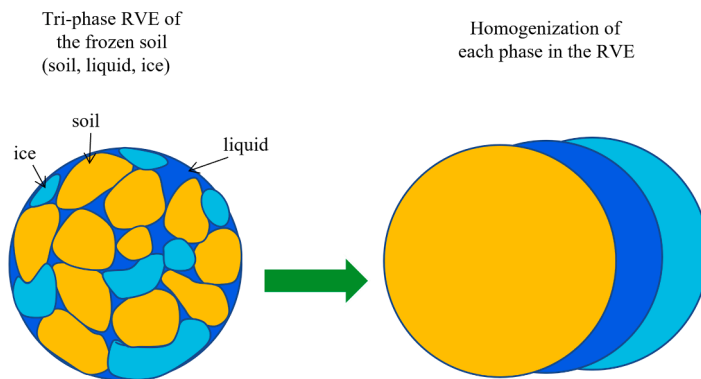


**Fig. 1.** Schematic diagram of a representative volume in a saturated frozen porous medium and its decomposition into three intrinsic phases and homogenizations (after [58]).

where  $\mathbf{v}_\alpha$  is the vector velocity of phase  $\alpha$ ;  $\mathbf{R}^{\beta\alpha}$  is the drag force vector between phases  $\alpha$  and  $\beta$  [16–18,52]. By expanding Eq. (6), the relative velocity terms between water and soil can be observed as follows:

$$\mathbf{w}_{ls} = \frac{\mathbf{k}_l}{n_l \gamma_l} (-\nabla p_l + \rho_l \mathbf{b}) \quad (7)$$

where  $\gamma_l$  is the unit weight of the liquid phase;  $\mathbf{w}_{ls}$  is the relative velocity between the solid phase and the water phase;  $\mathbf{k}_l$  is the water permeability vector, which is a function of porosity, pore water pressure and temperature (will be given in the next section). It is noted that the ice flux is insignificantly small and thus is usually disregarded [12,58].

On the other hand, by summing the general form of the linear momentum equation of each phase and neglecting the relative accelerations among the soil, water and ice [16–18,52], the momentum equation for the entire frozen mixture can be obtained [16–18, 52]:

$$\frac{d^s \mathbf{v}_s}{dt} = \frac{1}{\rho} \nabla \cdot \boldsymbol{\sigma} + \mathbf{b} \quad (8)$$

where  $\boldsymbol{\sigma}$  is the total Cauchy stress tensor; and  $\mathbf{b}$  is the gravity acceleration vector. To obtain the evolution of total stress, one needs to define a constitutive model to describe the evolution of constitutive stress with respect to strain and a governing equation for the evolution of pore water pressure, both of which are given in the next sections.

### 2.2.2. Mass balance equation

The general form of the mass balance equation for each phase  $\alpha$  in the frozen mixture considering the mass exchange between phases  $\beta$  and  $\alpha$  (i.e.,  $M^{\beta\alpha}$ , noting that the mass exchange only takes place between the liquid and ice phases in this paper) can be written as follows:

$$\frac{d^s \bar{\rho}_\alpha}{dt} + \rho^\alpha \nabla \cdot \mathbf{v}_\alpha + \sum_\beta M^{\beta\alpha} = 0 \quad (9)$$

Let us now consider the mass balance of the soil phase. The rate of change of local porosity can be obtained by substituting Eq. (1) into Eq. (9), giving:

$$\frac{d^s n}{dt} = (1 - n) \nabla \cdot \mathbf{v}_s \quad (10)$$

Similarly, the following mass balance equations for water and ice phases can be obtained by making use of Eqs. (1) and (9):

$$n S_r \frac{d^l \rho_l}{dt} + S_r \rho_l \frac{d^l n}{dt} + n \rho_l \frac{d^l S_r}{dt} + n S_r \rho_l \nabla \cdot \mathbf{v}_l = - \sum_l M^{il} \quad (11)$$

$$n S_i \frac{d^i \rho_i}{dt} + \rho_i S_i \frac{d^i n}{dt} + n \rho_i \frac{d^i S_i}{dt} + n_i \rho_i \nabla \cdot \mathbf{v}_a = - \sum_i M^{ii} \quad (12)$$

The summation symbol in the formulation indicates the total mass exchange between ice and water in an RVE. By converting the material derivatives of a field quantity on the water and ice phases to those on the solid phase, the following equations can be obtained:

$$n_l \frac{d^s \rho_l}{dt} + \mathbf{w}_{ls} \cdot \nabla \rho_l + S_r \rho_l \frac{d^s n}{dt} + n \rho_l \frac{d^s S_r}{dt} + \mathbf{w}_{ls} \cdot \nabla n_l + n_l \rho_l \nabla \cdot \mathbf{v}_l = - \sum_l M^{il} \quad (13)$$

$$n_i \frac{d^s \rho_i}{dt} + \mathbf{w}_{is} \cdot \nabla \rho_i + n \rho_i \frac{d^s S_i}{dt} + S_i \rho_i \frac{d^s n}{dt} + \mathbf{w}_{is} \cdot \nabla n_i + n_i \rho_i \nabla \cdot \mathbf{v}_i = - \sum_i M^{ii} \quad (14)$$

Making use of the mass balance equation for the solid phase in Eq. (10), Eqs. (13) and (14) become:

$$n_l \frac{d^s \rho_l}{dt} + S_r \rho_l \nabla \cdot \mathbf{v}_s + n \rho_l \frac{d^s S_r}{dt} + \nabla \cdot (n_l \rho_l \mathbf{w}_{ls}) = - \sum_l M^{il} \quad (15)$$

$$n_i \frac{d^s \rho_i}{dt} + S_i \rho_i \nabla \cdot \mathbf{v}_s + n \rho_i \frac{d^s S_i}{dt} + \nabla \cdot (n_i \rho_i \mathbf{w}_{is}) = - \sum_i M^{ii} \quad (16)$$

It is noted that mass exchange between the ice phase and water phase can be cancelled out, i.e.,  $\sum_l M^{il} + \sum_i M^{ii} = 0$ , thus the summation of Eqs. (15) and (16) yield the mass balance equation for the pores in the mixture as:

$$n_l \frac{d^s \rho_l}{dt} + n_i \frac{d^s \rho_i}{dt} + (S_r \rho_l + S_i \rho_i) \nabla \cdot \mathbf{v}_s + n \rho_l \frac{d^s S_r}{dt} + n \rho_i \frac{d^s S_i}{dt} + \nabla \cdot (n_l \rho_l \mathbf{w}_{ls}) + \nabla \cdot (n_i \rho_i \mathbf{w}_{is}) = 0 \quad (17)$$

Herein, by considering that the ice phase is fully incompressible [12,58], Eq. (17) becomes:



$$(S_r \rho_l + S_i \rho_i) \nabla \cdot \mathbf{v}_s + n_l \frac{d^s \rho_l}{dt} + n \rho_l \frac{d^s S_r}{dt} + n \rho_i \frac{d^s S_i}{dt} + \rho_l \nabla \cdot (n_l \mathbf{w}_{ls}) + \rho_i \nabla \cdot (n_i \mathbf{w}_{is}) = 0 \quad (18)$$

In general, the relative flow vector or relative velocity between ice and the soil skeleton  $\mathbf{w}_{is}$  is much slower than that between liquid and soil; thus, it can be assumed that  $\mathbf{w}_{is} \approx 0$  [12,58]. As a result, Eq. (18) can be simplified:

$$(S_r + S_i \eta) \nabla \cdot \mathbf{v}_s + \frac{n S_r}{K_l} \frac{d^s p_l}{dt} + n \frac{d^s S_r}{dt} + n \eta \frac{d^s S_i}{dt} + \nabla \cdot (n_i \mathbf{w}_{is}) = 0 \quad (19)$$

where  $\eta$  is the density ratio of ice and water;  $K_l$  is the equivalent bulk modulus of the fluid phase, which can be assumed as slightly compressible or fully incompressible. The fully incompressible assumption requires an appropriate integration method, which will be given in the next section.

Substituting Eq. (7) in Eq. (19) leads to:

$$(S_r + S_i \eta) \nabla \cdot \mathbf{v}_s + \frac{n S_r}{K_l} \frac{d^s p_l}{dt} + n(1 - \eta) \frac{d^s S_r}{dt} - \frac{1}{\gamma_l} \nabla \cdot [\mathbf{k}_l (\nabla(p_l - \rho_l \mathbf{b}))] = 0 \quad (20)$$

In saturated frozen soils, the degree of saturation is usually a function of cryogenic suction ( $s_i$ ) and pore-water pressure ( $p_l$ ); thus, further expansion of the third term in Eq. (20) leads to:

$$[S_r + S_i \eta] \nabla \cdot \mathbf{v}_s + [n(1 - \eta) C_i + C_s] \frac{d^s p_l}{dt} + n(1 - \eta) T_i \frac{d^s T}{dt} - \frac{1}{\gamma_l} \nabla \cdot [\mathbf{k}_l (\nabla(p_l - \rho_l \mathbf{b}))] = 0 \quad (21)$$

where

$$\begin{aligned} C_i &= \frac{d^s S_r}{ds_i} \frac{d^s s_i}{dp_l} \\ C_s &= \frac{n S_r}{K_l} \\ T_i &= \frac{d^s S_r}{ds_i} \frac{d^s s_i}{dT} \end{aligned} \quad (22)$$

To close Eq. (21), the energy balance equation for temperature changes and another two complementary equations for the degree of saturation and cryogenic suction are still required, which will be given in the later sections. On the other hand, when the frozen soil is fully thawed or unfrozen (i.e.,  $T > T_k$ ), the degree of saturation  $S_r$  in Eq. (20) become a constant, thus Eq. (21) is recovered back to the governing equation for the fluid phase in unfrozen saturated soil [19]:

$$\nabla \cdot \mathbf{v}_s + C_s^f \frac{d^s p_l}{dt} - \frac{1}{\gamma_l} \nabla \cdot [\mathbf{k}_l (\nabla(p_l - \rho_l \mathbf{b}))] = 0 \quad (23)$$

where  $C_s^f = \frac{n}{K_l}$  is the specific storage term of the saturated medium. The pore-water pressure in Eqs. (21) and (23) can be integrated using our recently proposed Three-Point-Integration (TPI) Scheme [17], which will be given in Section 4.4.

### 2.2.3. Energy balance equation

Besides the mass balance equation above, the energy balance equation is required to calculate the evolution of heat conduction. The general form of the energy balance equation for phase  $\alpha$  is given by [58]:

$$\bar{\rho}_\alpha \frac{d^a(e^\alpha)}{dt} + e^\alpha \left( - \sum_\beta M^{\beta\alpha} \right) + \Delta Q_\alpha^{ph} + \nabla \cdot \mathbf{q}^\alpha = 0 \quad (24)$$

where the second term  $e^\alpha \left( - \sum_\beta M^{\beta\alpha} \right)$  stands for the energy change caused by phase change from phase  $\beta$  to phase  $\alpha$ ; the third term  $\Delta Q_\alpha^{ph}$  is the additional energy causing the phase change;  $\mathbf{q}^\alpha$  is the conductive heat flux for phase  $\alpha$ ; and  $e^\alpha$  is the specific internal energy of phase  $\alpha$ , which is defined in terms of its heat capacity  $c_\alpha$  and temperature as follows:

$$e^\alpha := c_\alpha T \quad (25)$$

where  $c_\alpha$  represents the specific heat capacity of phase  $\alpha$ .

Thereafter, the energy balance equations for solid, water and ice can be written as follows:

$$n_s \rho_s \frac{d^s e^s}{dt} + \nabla \cdot \mathbf{q}^s = 0 \quad (26)$$

$$n_l \rho_l \frac{d^s e^l}{dt} + n_l \rho_l \mathbf{w}_{ls} \cdot \nabla e^l + e^l \left( - \sum_i M^{il} \right) + \Delta Q_i^{ph} + \nabla \cdot \mathbf{q}^l = 0 \quad (27)$$

$$n_i \rho_i \frac{d^s e^i}{dt} + n_i \rho_i \mathbf{w}_{is} \cdot \nabla e^i + e^i \left( - \sum_i M^{ii} \right) + \Delta Q_i^{ph} + \nabla \cdot \mathbf{q}^i = 0 \quad (28)$$

It is noted that  $\Delta Q_i^{ph} + \Delta Q_i^{ph} = 0$  and the difference between  $e^l (\sum_i M^{il}) + e^i (\sum_i M^{ii})$  indicates the extra latent heat for the mass exchange associated with phase change, which can be represented by the change in the degree of saturation [58]. Thereafter, making use of Eqs. (24) - (28), the following energy balance equation for the entire mixture can be obtained:

$$(\rho c)_{eff} \frac{dT}{dt} + (\rho c)_{adv} \mathbf{w}_{ls} \cdot \nabla T + \frac{n_l \rho_l}{\rho_l S_r + \rho_i S_i} L_f \frac{d^s S_r}{dt} + \nabla \cdot (\lambda_{eff} \nabla T) = 0 \quad (29)$$

where  $(\rho c)_{eff} = c_s n_s \rho_s + c_l n_l \rho_l + c_i n_i \rho_i$  is the effective heat capacity for the mixture;  $(\rho c)_{adv} = c_l \rho_l + S_i / S_r c_i \rho_i$  is the advective heat transfer coefficient determined only on the heat capacity of the liquid and ice phases [58];  $L_f$  is the latent heat of the fusion of ice. It is noted here an isotropic heat conduction is considered in this study.

The second term in Eq. (29) represents the advection heat conduction with  $\mathbf{w}_{ls}$  being the relative velocity between the solid and the water phase. The third term stands for the heat consumption for phase change between water and ice, and the last term is the heat diffusion, where the overall effective conductivity of the mixture can be obtained by simply averaging the conductivity for each phase using the following forms:

$$\lambda_{eff} = \lambda_s^{1-n} \lambda_l^{n S_r} \lambda_i^{n S_i} \quad (30)$$

where  $\lambda_s$ ,  $\lambda_l$  and  $\lambda_i$  denote the intrinsic thermal conductivities of the solid phase, liquid phase and ice phase, respectively. To close the above governing equation, one needs to define a hydraulic constitutive model for the relation between pore water pressure, cryogenic suction and the degree of saturation, which will be given in the next section.

### 2.3. Complementary equations

#### 2.3.1. Clausius-Clapeyron equation

The general Clausius-Clapeyron equation is adopted to describe the thermodynamic equilibrium between ice and unfrozen water. Thus, the cryogenic suction can be obtained in this equation, which is given as:

$$s_i = p_i - p_l \approx -L_f \rho_i \ln \left( \frac{T}{T_k} \right) \quad (31)$$

where  $T_k (= 273.15 \text{ K})$  is the freezing point of bulk water. It is noted that the cryogenic suction is a function of temperature in the frozen soil, and the influence of water pressure on the magnitude of cryogenic suction is significantly small.

An additional equation is required to determine the water saturation when knowing the magnitude of cryogenic suction. In this study, the Soil Water Retention Curve (SWRC) given by van Genuchten (1980) [60] is adopted, which reads:

$$S_r = S_{imax} [1 + (g_a S_i)^{g_n}]^{g_c} \quad (32)$$

Eq. (32) is also known as the soil freezing characteristic curve (SFCC) [4], where  $S_{imax}$  denotes the maximum degree of ice

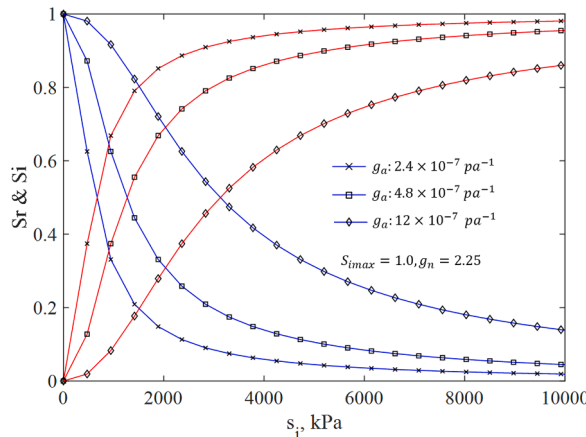


Fig. 2. Schematic diagram of the SWRC with the blue line denoting  $S_r$  and red lines denoting  $S_i$ .

saturation, which is roughly 1 when disregarding the air phase;  $g_a$ ,  $g_n$  and  $g_c = (g_n - 1)/g_n$  are three fitting parameters [60]. The relationship between cryogenic suction and the degree of saturation is given in Fig. 2, where the change in the degree of saturation against cryogenic suction is plotted for different model parameters, representing the hydraulic behaviour of various types of frozen soils during freezing or thawing.

Noted that cryogenic suction is a function of temperature; thus, the governing equation in Eq. (29) can be further written as:

$$(\rho c)_{eff} \frac{dT}{dt} + (\rho c)_{adv} \mathbf{w}_{ls} \cdot \nabla T + c L_f C_i \frac{dT}{dt} + \nabla \cdot (\lambda_{eff} \nabla T) = 0 \quad (33)$$

where  $c = \frac{n \rho_l \rho_i}{\rho_l S_r + \rho_i S_i}$  is the density-normalised volumetric parameter;  $C_i$  is the non-isothermal water capacity, which is defined by the derivative of the degree of saturation with respect to temperature. It is noted that in some studies, an apparent heat capacity  $c_f = (\rho c)_{eff} + n L_f C_i$  is considered, where the density-normalised volumetric parameter  $c$  in Eq. (33) is simplified as the porosity [12,58]. This consideration will lead to the same governing equation of the form (33). The only difference lies in how to interpret the heat capacity of frozen soil  $(\rho c)_{eff}$  and latent heat of fusion term  $n L_f C_i$ . This study still stays with the density-normalised volumetric parameter in Eq. (33).

The permeability function is also given as follows [59]:

$$\mathbf{k} = \mathbf{k}_{sat}(e) S_e^{g_l} \left[ 1 - \left( 1 - S_e^{\frac{1}{g_c}} \right)^{g_c} \right]^2 \quad (34)$$

$$\mathbf{k}_{sat}(e) = \mathbf{k}_{sat}^0 \exp \left( \frac{e - e_0}{C_k} \right) \quad (35)$$

where  $S_e = \frac{S_r - S_{rmin}}{S_{rmax} - S_{rmin}}$  is the effective degree of saturation, with  $S_{rmax}$  and  $S_{rmin}$  denoting the maximum and minimum degree of saturation;  $\mathbf{k}_{sat}(e)$  is the saturated water permeability vector;  $e$  and  $e_0$  is the current and initial void ratios; and  $C_k$  is the Kozeny-Carman coefficient that determines the variation ratio of the saturated permeability with the void ratio. A table summarising the governing equations and their implementations will be given at the end of Section 4.

### 3. A CASM-F constitutive model for frozen soil

#### 3.1. Stress-strain increment

Several constitutive models using different constitutive stress variables have been proposed to model frozen soils [4,10,12,61,62]. For example, Nishimura and his co-worker [4] adopted the net-stress and cryogenic suction to formulate the two-stress variable constitutive relationship within the Modified Cam-Clay (MCC) model for frozen soil. Based on the same MCC framework, Ghoreishian Amiri and his co-workers [10] proposed using solid-phase stress as the constitutive stress, which was later followed by other researchers [62]. Bishop-type effective stress has also been discussed [12,61] in the constitutive modelling of frozen soil. Among these stress approaches, the solid-phase stress is preferred in this study, considering its ease of implementation and the capability of describing a smooth transition from the frozen state to the unfrozen stage and vice versa. The solid-phase stress is defined as follows [10]:

$$\boldsymbol{\sigma}^* = \boldsymbol{\sigma} - S_r p_l \mathbf{I} \quad (36)$$

where  $\boldsymbol{\sigma}$  is the total Cauchy stress tensor. The incremental form of the solid-phase stress reads:

$$d\boldsymbol{\sigma}^* = \mathbf{D} : (d\boldsymbol{\epsilon} - d\boldsymbol{\epsilon}^{mp} - d\boldsymbol{\epsilon}^{sp}) \quad (37)$$

where  $d\boldsymbol{\epsilon}$  is the total mechanical strain increment, including the thermal strain increment  $d\boldsymbol{\epsilon}^T$ ;  $d\boldsymbol{\epsilon}^{sp}$  is the plastic strain increment caused by suction;  $d\boldsymbol{\epsilon}^{mp}$  stands for plastic strains due to mechanical load.  $\mathbf{D}$  is the constitutive tangent stiffness tensor. In 2D plane strain condition, it is defined as:

$$\mathbf{D} = \begin{bmatrix} D_0(1-\nu) & D_0\nu & D_0\nu & 0 \\ D_0\nu & D_0(1-\nu) & D_0\nu & 0 \\ D_0\nu & D_0\nu & D_0(1-\nu) & 0 \\ 0 & 0 & 0 & D_0(1-2\nu) \end{bmatrix}, \quad (38)$$

$$D_0 = \frac{3K}{1+\nu}, \quad K = \frac{(1+e)}{\kappa} p^* + (1-S_r)K_i$$

where  $p^*$  is the current mean constitutive stress;  $\nu$  is the Poisson's ratio;  $\kappa$  is the swelling index;  $K$  is the bulk modulus with  $(1-S_r)K_i$  denoting the increase of the overall bulk modulus in the soil mixture upon freezing, which varies from different soil materials and temperatures and thus requires experiment calibrations [10].

The plastic strain increments are as follows, respectively:

$$d\epsilon^{mp} = d\lambda_m \frac{\partial g_m}{\partial \sigma^*} \quad (39)$$

$$d\epsilon^{sp} = -d\lambda_s \frac{\partial f_s}{\partial s_i} \mathbf{I}$$

where  $d\lambda_\gamma$  ( $\gamma = m, s$ ) is the plastic multiplier, and the subscripts  $m$  and  $s$  indicate the mechanics and suction, respectively;  $f_s$  is the suction-induced (SI) yield surface; and  $g_m$  is the potential flow function of the LC yield surface, which will be defined later.

Once the plastic strains are determined, the solid phase stresses are updated using the following relation:

$$d\sigma^* = \mathbf{D} : (d\epsilon - d\epsilon^{mp} - d\epsilon^{sp}) - \sigma^* : d\omega + d\omega : \sigma^* \quad (40)$$

where  $d\omega$  is the spin rate tensor. In the above equation, the Jaumann stress rate has been adopted to maintain the stress invariance under to rigid-body motion. This is essential for large deformation modelling because the proposed computational framework is still written using the infinitesimal strain theory. Although the Jaumann stress rate does not exactly preserve the objective measurement of the stress under very large deformation [24], its use in the current SPH simulations is acceptable. This is because SPH often requires very small timesteps to integrate its governing equations, thus limiting accumulation of objectivity errors. It has been demonstrated to be sufficient for modelling large deformation in many previous studies [15,24,28,30,32]. For more rigorous treatment of large deformation, multiplicative elastoplasticity theory may be used, as demonstrated in [26]; however, that approach is out of the scope of this study.

### 3.2. CASM-F model for frozen soil

Most existing constitutive models for frozen soil are based on the MCC model [4,10,12,61]. To further advance the constitutive modelling of frozen soils, the Clay and Sand model (CASM), originally proposed by Yu (1998) [63], is chosen as the base model for developing a new constitutive model for frozen soil, referred to here as CASM-F. The CASM-F model extends the original CASM framework to incorporate the influences of ice and thermal factors on the volumetric and shear strength behaviours of frozen soil. Additionally, a simple subloading yield surface is incorporated into the model to obtain a smooth elastic-plastic transition, which will be documented in the next section.

Fig. 3 presents the reference yield surface (RYS) of the CASM-F model, which is expressed as follows:

$$f_m = \left( \frac{q}{M(p^* + p_s)} \right)^{n_c} + \frac{1}{\ln r_c} \ln \left( \frac{p^* + p_s}{p_0^*(s_i) + p_s} \right) \quad (41)$$

where  $p^*$  is the mean solid-phase pressure;  $q$  is the deviatoric pressure computed from the solid-phase stress;  $p_s (= -k_t s_i)$  denotes the cohesion raised by cryogenic suction;  $M$  is the slope of the Critical State Line (CSL);  $n_c$  and  $r_c$  are two fitting parameters defining the shape of the yield surface in the CASM model;  $p_0^*(s_i)$  is the pre-consolidation pressure at the frozen stage. The pre-consolidation pressure  $p_0^*(s_i)$  is a function of cryogenic suction, which can be defined as follows:

$$p_0^*(s_i) = P_r \left( \frac{p_0^*}{P_r} \right)^{\frac{\lambda_0 - \kappa}{\lambda(s_i) - \kappa}} \quad (42)$$

where  $P_r$  is the reference pressure;  $p_0^*$  is the pre-consolidation pressure at the unfrozen saturated state;  $\lambda_0$  and  $\kappa$  are the compression and swelling indexes, respectively; and  $\lambda(s_i)$  stands for the change of the compression index with cryogenic suction in frozen soil, which can

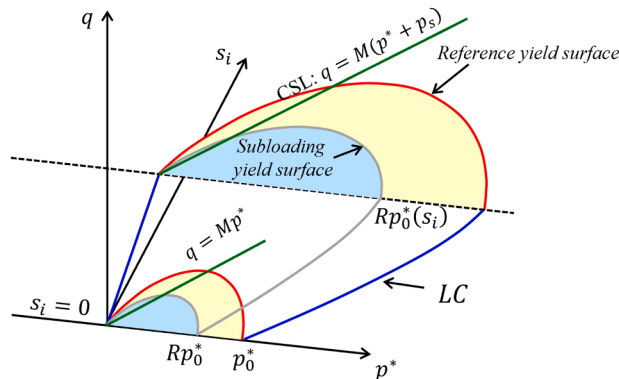


Fig. 3. Schematic diagram of the yield surface of the CASM-F model for frozen soil.

be given as:

$$\lambda(s_i) = \lambda_0[(1-r)\exp(-\beta s_i) + r] \quad (43)$$

Eqs. (42) and (43) defined the loading collapse (LC) curve, with  $r$  and  $\beta$  being two constants related to the maximum stiffness of soil [64]. While this hardening law has been widely adopted, it does have known limitations, particularly in the context of unsaturated soils [64–68]. One notable issue is the predicted divergence of the normal compression line (NCL) with increasing suction, whereas experimental observations have shown that, under high confining pressures, NCLs for different matric suction levels tend to converge due to void closure and pressurised saturation phenomenon [68,69]. However, these concerns are primarily relevant to unsaturated soils and may not necessarily apply to frozen soils. Unlike unsaturated soils, where compressibility is affected by air-filled voids, the pore void spaces in frozen soil mixture are fully occupied by water and ice, both of which are nearly incompressible. This fundamental difference in pore structure alters the mechanical response of frozen soils, making the divergence of the NCL less critical for frozen soils modelling. It is also worth pointing out that the above hardening law has been shown to be suitable for unsaturated soils under low confining stress conditions, which are typical of many practical applications [67,68]. Additionally, the NCL divergence can be mitigated by considering appropriate parameters within the hardening framework, as discussed by Wheeler et al. (2002) [70]. Importantly, this adopted hardening law offers a straightforward and consistent way to predict key features observed in both unsaturated soils [64, 67] and frozen soils [4,10,62]. Given these considerations, we consider it suitable for the scope of this paper. We leave further refinement with alternative hardening laws [65,67,70,71] to our future work.

To define the stress ratio and dilatancy ratio relationship, this study adopts the well-known Rowe's stress-dilatancy relation, originally proposed by Rowe [72] and later adopted in the original CAMS by Yu [63]:

$$D = \frac{de_v^p}{de_q^p} = \frac{9(M-\eta)}{9+3M-2M\eta} \quad (44)$$

where  $D$  is known as the dilatancy ratio;  $de_v^p$  and  $de_q^p$  are the volumetric and deviatoric plastic strain increments;  $\eta$  is the stress ratio between deviatoric stress and mean stress.

This stress-dilatancy rule indicates that the current model follows a non-associated plastic flow rule, with a plastic potential function  $g_m$  satisfying:

$$\frac{\partial g_m}{\partial p^*} = D, \quad \frac{\partial g_m}{\partial q} = 1 \quad (45)$$

The hardening law for the LC yield surface is defined as follows:

$$dp_0^* = \frac{P_0^*}{\lambda_0 - \kappa} v_e (S_r de_v^{sp} + de_v^{mp}) \quad (46)$$

where  $v_e$  is the specific volume and  $S_r$  is the degree of saturation. The hardening relation adopted here is based on the coupling hardening approach proposed by [64], in which suction-induced plastic expansion leads to a reduction in the pre-consolidation pressure  $p_0^*$ , scaled by the water saturation. This indicates that higher water content will result in more expansion and consequently, more reduction in  $p_0^*$  [10]. Alternatively,  $S_r$  can be replaced by the coupling parameters to provide a more stable representation of the interaction between the suction-induced (SI) curve and the loading-collapse (LC) curve [73]. However, this refinement is not considered in the present study.

In addition to the LC yield surface, a so-called suction increase (SI) curve is introduced to capture the irreversible strain (or plastic volumetric expansion) [64] caused by ice segregation. This criterion is expressed as:

$$f_s = s_i - s_0 \quad (47)$$

where  $s_0$  is known as the maximum previous cryogenic suction, acting as the threshold for ice segregation. An associated flow rule is considered for the SI yield surface. The corresponding hardening law is given by:

$$ds_0 = -\frac{s_0 + P_{atm}}{\lambda(s_i) - \kappa_s} v_e (de_v^{sp} + S_r de_v^{mp}) \quad (48)$$

where  $\kappa_s$  is the swelling index at a frozen state. The performance of the model will be given in the next section.

### 3.3. Sub-loading yield surface framework

Classical plasticity models, including the Cam-clay and CASM models, typically assume that plastic deformation occurs only when the stress path reaches the yield surface. This assumption limits their ability to capture the smoothed transition from elastic to plastic behaviour observed in soil materials [74,75]. To overcome this limitation, a subloading yield surface (see Fig. 3) is introduced in the proposed model. Unlike the RYS, which defines the conventional onset of plasticity, the subloading surface always passes through the current stress state and remains enclosed within the RYS. This approach enables plastic strain to accumulate gradually, even before the stress state reaches the RYS, thereby better capturing the observed smooth transition. The subloading surface is defined as follows:

$$f_m = \left( \frac{q}{M(p^* + p_s)} \right)^{n_c} + \frac{1}{\ln r_c} \ln \left( \frac{p^* + p_s}{R p_0^*(s_i) + p_s} \right) \quad (49)$$

where  $R$  is the size ratio between the subloading yield surface and the reference yield surface.

The evolution of the subloading yield surface is governed by:

$$dR = (1 - R)R_0 \left( de_v^p + de_q^p \right) \quad (50)$$

where  $R_0$  is a material parameter controlling the rate at which the subloading yield surface expands toward the RYS and can be calibrated from the experimental data. It is important to note that, unlike subloading frameworks developed for cyclic loading conditions [74,75], the present formulation is intended solely for monotonic loading. The unloading process is assumed to be purely elastic. The performance of the proposed subloading scheme will be demonstrated in the next section.

### 3.4. Performance of the CASM-F model

#### 3.4.1. Constitutive response under different loading paths

Before implementing the CASM-F model in SPH for simulating thermal thawing-induced slope failure, it is necessary first to examine its performance in predicting cryogenic suction-stress-strain response under specific loading paths. To achieve this goal, two typical stress paths representing the potential failure mechanisms in frozen soil are considered, as depicted in Fig. 4.

Fig. 4(a) illustrates the first loading path, depicting a typical failure behaviour observed in laboratory triaxial tests. In this scenario, the soil sample is initially frozen (path AB), then subjected to an isotropic loading (BC) to a certain net pressure level  $p_n$ , followed by an unloading process (CD). Next, the temperature is increased to simulate the thawing process (DE), after which the sample is sheared until failure (EF). Fig. 4(b) presents the second stress loading path, representing a more common thawing-induced failure mechanism in a slope. Here, failure occurs as a result of thawing after a combination of loading conditions, including freezing (AB), isotropic loading (BC), unloading (CD), and a pre-shearing state (DE) before the thawing loading (EF). The constitutive parameters for both cases are given in Table 1. These constitutive parameters have been calibrated in the experimental triaxial tests [62].

The predicted suction-stress-strain response to the designed stress path (a) is shown in Fig. 5, demonstrating that the model captures several key features of the frozen soil behaviour. For example, as the temperature drops from 0 to  $-3^\circ\text{C}$  (path AB), cryogenic suction develops within the soil. During the early freezing stage (AB'), the cryogenic suction acts to bond the soil grains together, causing an elastic compression and an associated increase in solid-phase stress (Fig. 5(b)). Beyond point B', the freezing segregation point, further increases in cryogenic suction trigger the ice segregation, resulting in freezing heave and significant volumetric expansion (see path B'B in Fig. 5(b)). It is noted here this significant volume expansion is primarily attributed to ice segregation, a well-known process in freezing soils wherein unfrozen water is driven toward the freezing front under the cryogenic suction gradient, promoting the formation of ice lenses that expand the soil volume. This process can be repeated as long as liquid water continues to migrate, resulting in significant heave, despite the relatively minor volumetric change associated with the water-to-ice phase transition. To quantify this expansion in the field, laboratory calibration is required to determine appropriate parameters for the SI yield

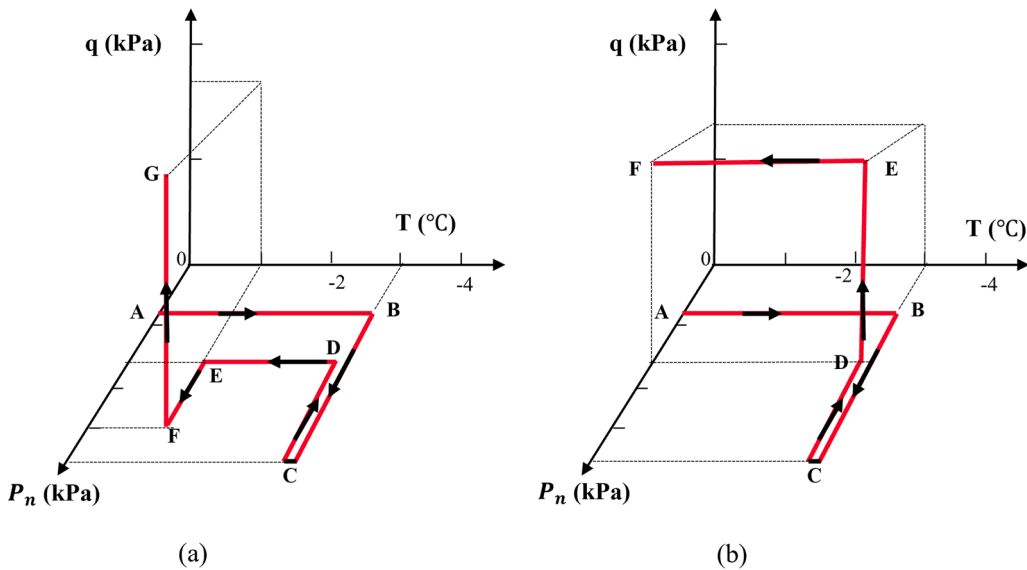
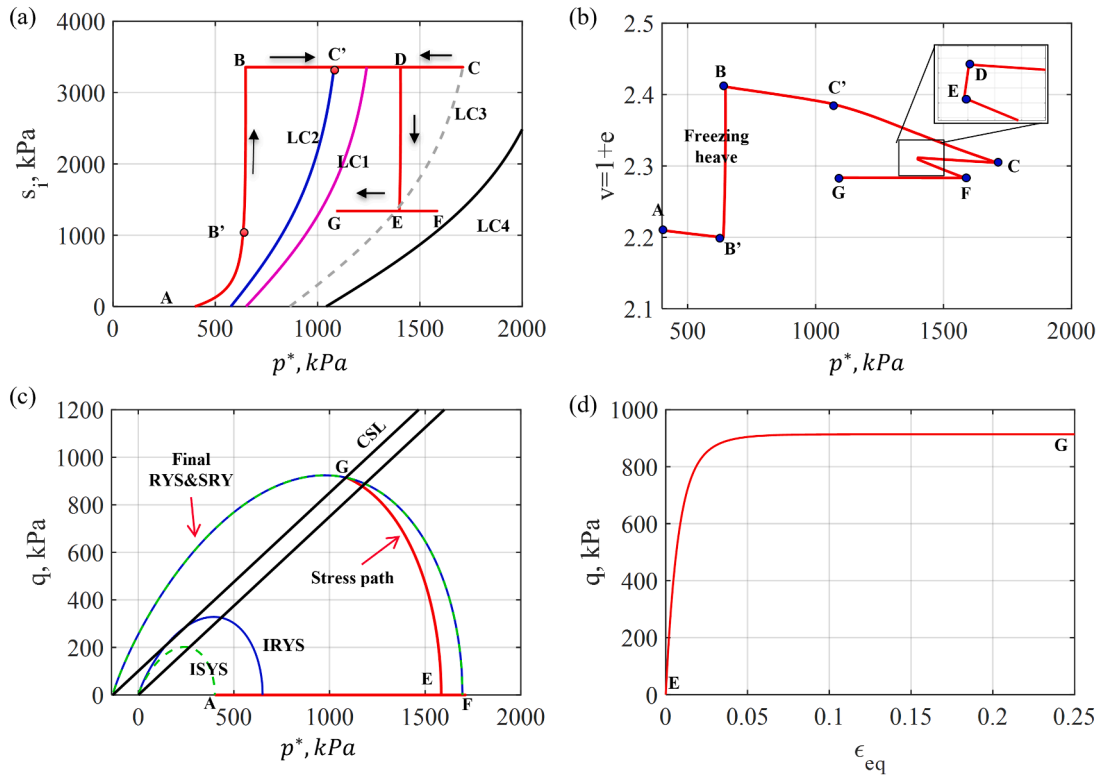


Fig. 4. Response of the CASM-F Model to two loading paths in which failure can occur: (a) Shearing-induced failure of frozen soil; (b) Field thawing-triggered failure.

**Table 1**  
Constitutive parameters.

	Parameters	Symbol	Value
Mechanical properties	Compression index	$\lambda_0$	0.25
	Swelling index	$\kappa$	0.05
	SI parameter	$\kappa_s$	0.001
	Freezing bring-up Stiffness (MPa)	$K_i$	30
	Poisson's ratio	$\nu$	0.33
	Slope of CSL	$M$	0.75
	Bring-up cohesion parameter	$k_t$	0.1
	Segregation threshold (MPa)	$s_0$	1.2
	LC stiffness coefficient	$r$	0.9
	LC stiffness coefficient ( $\text{Pa}^{-1}$ )	$\beta$	$0.825 \times 10^{-6}$
	Initial pre-consolidation pressure (MPa)	$p_0^*$	0.65
	Reference pressure (MPa)	$P_r$	0.005
	Constitutive parameter	$r_c$	1.75
	Constitutive parameter	$n_c$	2.0
	Initial void ratio	$e_0$	1.21
	Subloading parameter	$R_0$	100
	Freezing point ( $^{\circ}\text{C}$ )	$T_k$	0.0
Thermal properties	SFWC parameter ( $\text{Pa}^{-1}$ )	$g_a$	$3.33 \times 10^{-6}$
Hydraulic properties	Maximum ice saturation	$S_{imax}$	1.0
	SFWC parameter	$g_n$	1.25
	SFWC parameter	$g_c$	0.85



**Fig. 5.** Response of the CASM-F to the design stress path (a). (a) Stress path in  $p^* - s_i$  plane; (b) Stress path in the volumetric plane; (c) Evolution of yield surface; (d) Stress-train curve.

surface.

The plastic expansion induced by ice segregation softens the soil structure, shifting the initial LC curve leftwards from LC1 (marked by pink) to LC2 (marked by blue), as shown in Fig. 5(a). During the subsequent compression stage (BC), yielding is observed at point C' on LC2, followed by a significant contraction in the pore void among path C'C in Fig. 5(b), shifting further the loading collapse curve from LC2 to LC3. It is noted here that, due to the subloading yield surface, a smooth transition from elastic state to plastic at point C' is achieved. During unloading (CD), only a minor amount of elastic deformation is recovered. In the thawing stage (DE), the decrease in



suction reduces solid-phase stress, resulting in slight compression along path DE (Fig. 5(b)). This minor compression is likely due to the reduction of stiffness upon thawing. Since the stress path remains within the LC3 region, this deformation is just elastic. After thawing, the sample undergoes additional confinement along path DE before undrained shearing is applied until failure, and the corresponding stress-strain curve is given in Fig. 5(d). The stress path in the  $p^* - q$  plane and the corresponding evolution of the initial reference yield surface (IRYS) and subloading yield surface (ISRS) are presented in Fig. 5(c).

The predicted cryogenic suction-stress-strain response for stress path (b) is shown in Fig. 6. After undergoing freezing AB, consolidation BC, and unloading CD, a pre-shear condition before thawing failure is imposed to simulate the typical stress state in the frozen soil on a slope (path DE in Fig. 6(c)). This results in a small equivalent deviatoric shear strain along DE in the  $\epsilon_{eq} - s_i$  plane (Fig. 6(d)). Due to yield on the subloading yield surface, the stress path DE goes slightly to the left, indicating plastic shearing contraction. Thawing is then simulated by increasing the temperature from  $-3$  to  $-0.08^\circ\text{C}$  until failure. As the temperature rises to  $-2^\circ\text{C}$ , the reduction of cryogenic suction causes the shrinkage of the reference yield surface, which coincides with the subloading yield surface at point F'. During this process EF', slight deviatoric strain develops, indicating failure is about to occur. Continued heating introduces further shrinkage, driving the stress state beyond both reference and subloading yield surfaces and triggering failure, as evidenced by the rapid development of deviatoric strain (F'F) in Fig. 6(d), indicating the soil fails at a cryogenic suction level of around 0.1 MPa. Additionally, significant volumetric contraction occurs (path EF in Fig. 6(b)), a phenomenon often referred to as thawing collapse.

### 3.4.2. Validation of the constitutive model against experimental tests

In this section, the performance of the constitutive model is validated against experimental data. A series of triaxial tests on frozen sandy soil samples under a confining pressure of 1 MPa at different temperatures ( $-1^\circ\text{C}$ ,  $-2^\circ\text{C}$ ,  $-5^\circ\text{C}$  and  $-10^\circ\text{C}$ ) were reported by Xu et al. (2016) [76]. In their experiments, a dry sample was first placed in a rigid mould to prevent radial heaving during freezing and then saturated in a closed vacuum container. The sample was quickly frozen to the target temperature before being placed on the triaxial test machine, where it was subjected to a confining pressure of 1 MPa, and loaded until failure at a rate of 1.25 mm/min. The experimental data for the stress-strain relationship and volumetric behaviour data from Xu et al. [76] were presented in Fig. 7, marked by the different markers representing different temperatures.

To predict the frozen soil behaviour in these experiments, constitutive model parameters were first calibrated. The CASM-F model requires a complete set of parameters, which can be determined based on multiple types of experimental data. Specifically, soil water freezing test data are required for calibrating the hydraulic constitutive parameters, while triaxial and consolidation test data are needed to determine the rest of the mechanical parameters. In this study, several physical parameters were adopted from the work of

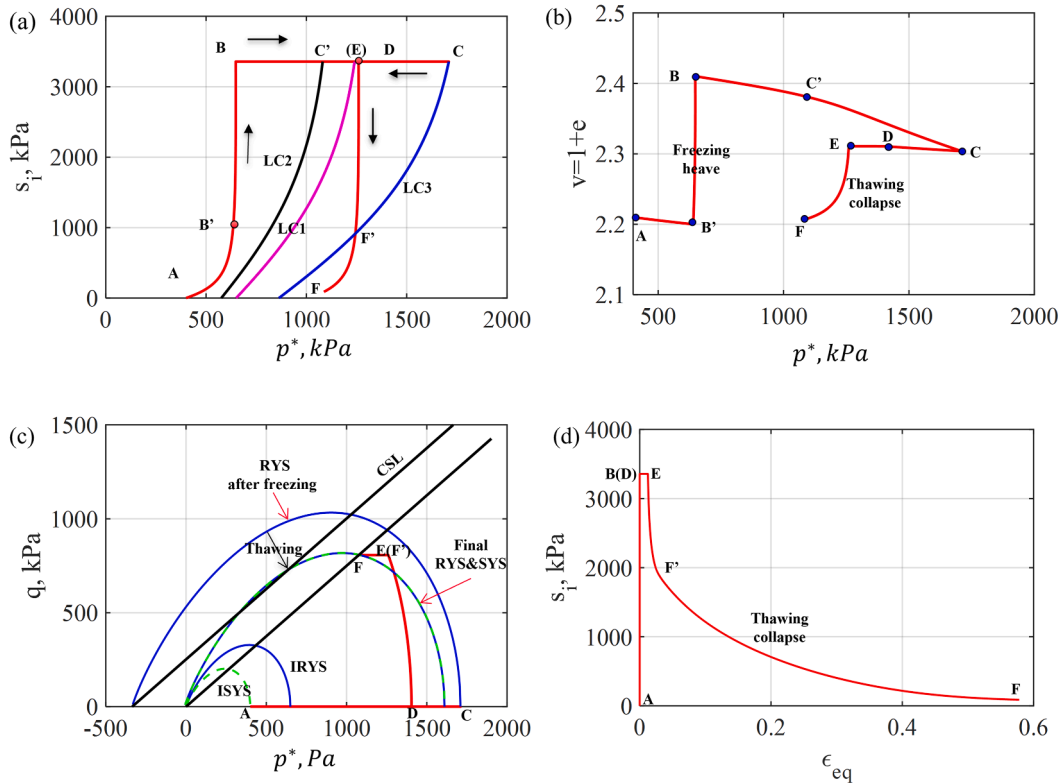


**Fig. 6.** Response of the CASM-F to the design stress path (b). (a) Stress path in the  $p^* - s_i$  plane; (b) Stress path in the volumetric plane; (c) Evolution of yield surface; (d) Suction-shear strain curve.

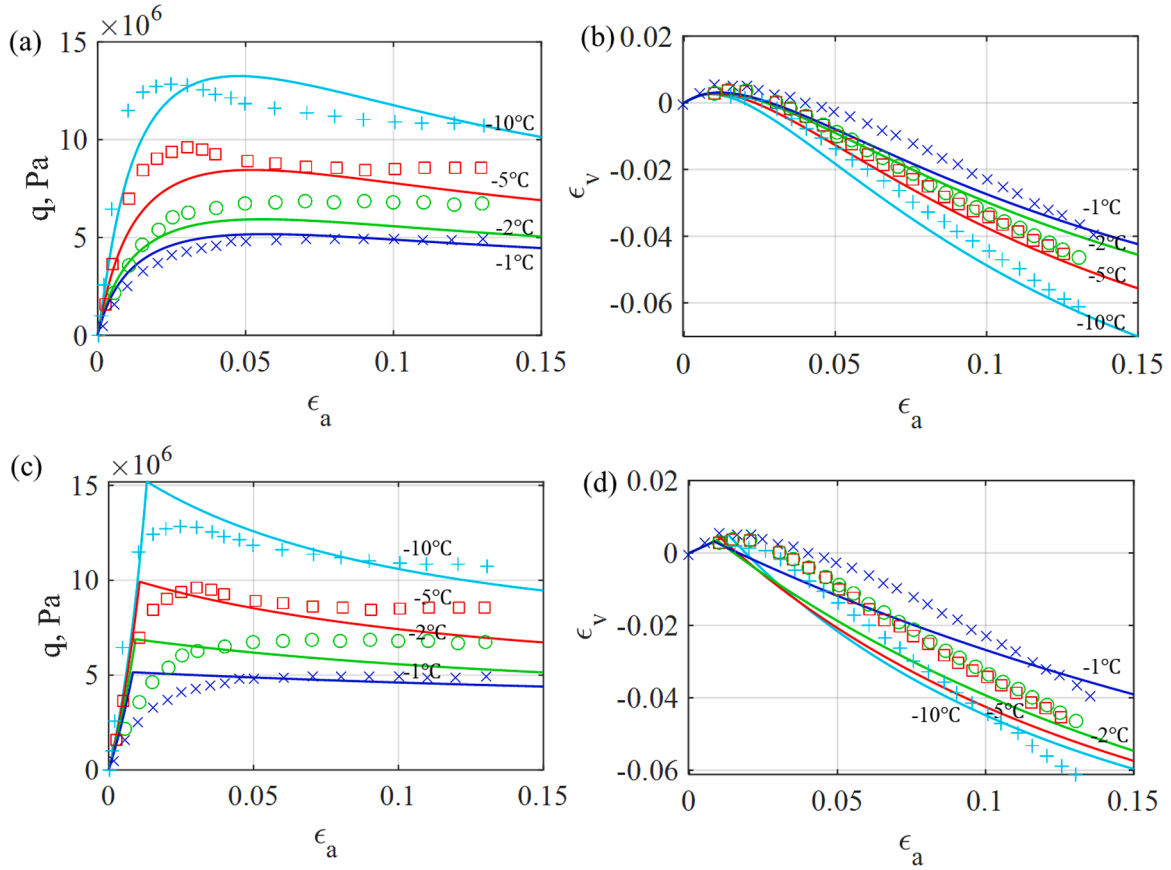


**Fig. 7.** Prediction of the triaxial test results on frozen soil under different temperatures using the CASM-F model (Markers: Experimental data extracted from [76]; Solid lines: Model prediction) (a-b): Prediction using the subloading yield surface model; (c-d): Prediction without using the subloading yield surface model.

**Table 2**  
Calibrated constitutive parameters.

	Parameters	Symbol	Value
Mechanical properties	Compression index	$\lambda_0$	0.22
	Swelling index	$\kappa$	0.02
	SI parameter	$\kappa_s$	0.002
	Freezing bring-up stiffness (MPa)	$K_i$	200
	Poisson's ratio	$\nu$	0.31
	Slope of CSL	$M$	1.5
	Bring-up cohesion parameter	$k_t$	0.125
	Segregation threshold (MPa)	$s_0$	11.33
	LC stiffness coefficient	$r$	0.625
	LC stiffness coefficient ( $\text{Pa}^{-1}$ )	$\beta$	$0.088 \times 10^{-6}$
	Initial pre-consolidation pressure (MPa)	$p_0^*$	7.55
	Reference pressure (MPa)	$P_r$	0.1
	Constitutive parameter	$r_c$	2.0
	Constitutive parameter	$n_c$	1.85
	Initial void ratio	$e_0$	0.8
	Subloading parameter	$R_0$	50
Thermal properties	Freezing point ( $^{\circ}\text{C}$ )	$T_k$	0.0
Hydraulic properties	SFWC parameter ( $\text{Pa}^{-1}$ )	$g_a$	$3.33 \times 10^{-6}$
	Maximum ice saturation	$s_{imax}$	1.0
	SFWC parameter	$g_n$	0.75
	SFWC parameter	$g_c$	0.85

Xu et al. (2016) [76]. However, due to the incompleteness of their experimental data, some parameters required by the model were not available and therefore had to be calibrated separately. This calibration was performed using experimental curves at  $-1^\circ\text{C}$ . The calibrated parameters were then used, without further adjustment, to predict the frozen soil behaviour at other temperatures (i.e.,  $-2^\circ\text{C}$ ,  $-5^\circ\text{C}$ , and  $-10^\circ\text{C}$ ), as listed in Table 2. Fig. 7(a) and (b) compare the stress-strain curves and volumetric behaviour data captured by the proposed model with the experimental data.

The proposed model closely predicts the stress-strain curves at different temperatures, as shown in Fig. 7(a), and effectively captures the increasing dilation behaviour as the temperature decreases, as illustrated in Fig. 7(b), showing good agreement with the experimental data of Xu et al. [76]. For example, in the experiment, as the temperature decreases, pore water freezes to form ice, which acts as a cementing agent, bonding soil particles and enhancing shear strength. This behaviour is well captured by the model thanks to the definition of pre-consolidation pressure, which governs the size of the yield surface and peak shear strength, as a function of cryogenic suction and temperature. As the temperature decreases, the increase in cryogenic suction expands the yield surface in the proposed model, thereby enhancing the peak strength of frozen soil. Notably, a smoothed elastic-plastic transition is achieved, thanks to the proposed subloading yield surface, outperforming the one that is without the subloading yield surface, as given in Fig. 7(c) and (d), where the overestimated peak strength is observed. Minor differences are observed at  $-10^\circ\text{C}$ , likely due to the increasing influence of ice properties, making precise prediction more challenging. Nevertheless, the model captures fairly well the strength variation across temperatures, particularly the softening behaviour at lower temperatures, as shown in Fig. 7(a). Overall, these results demonstrate that the CASM-F model can predict essential features of frozen soil under different temperatures, suggesting that the model is ready to be used to predict thawing-induced slope failure in SPH.

#### 4. SPH discretization of the governing equations and integration

##### 4.1. A brief overview of SPH

In SPH, the computation domain is discretised into a set of particles, with each particle carrying field quantities, including mass, density, velocity and pressure [15,24]. These field quantities and their first- and second-derivatives are obtained through a weighted summation process, utilising information from surrounding particles within the supporting domain of a weighting function [15,18,77–80]. To illustrate this, consider an arbitrary field quantity function  $f(\mathbf{x})$  at a specific position  $\mathbf{x}$ . The SPH approximations for function  $f(\mathbf{x})$ , along with its first and second derivatives are given as follow [18,81,82]:

$$\langle f(\mathbf{x}_i) \rangle = \sum_{j=1}^N V_j f(\mathbf{x}_j) W(\mathbf{x}_i - \mathbf{x}_j, h_{sml}) \quad (51)$$

$$\nabla_i^m f(\mathbf{x}_i) = \sum_{j=1}^N V_j [f(\mathbf{x}_j) - f(\mathbf{x}_i)] \hat{\nabla}_i^m W_{ij} \quad (52)$$

$$\frac{\partial^2 f_i}{\partial x^m \partial x^n} = \sum_{j=1}^N V_j (f_j - f_i) \mathcal{D}^{mn} \tilde{F}_{ij} - \frac{\partial f_i}{\partial r^m} \sum_{j=1}^N V_j r_{ji}^{m'} \mathcal{D}^{mn} \tilde{F}_{ij} \quad (53)$$

where the angle bracket  $\langle \rangle$  indicates the kernel approximation operator;  $V_j$  is the particle volume of  $j$ ;  $W(\mathbf{x}_i - \mathbf{x}_j, h_{sml})$  is a weighted smoothed kernel function;  $\hat{\nabla}_i^m W_{ij} = L_{ij}^{mn} \nabla_i^n W_{ij}$  is a corrected kernel gradient with  $L_{ij}^{mn} = \left[ \sum_{j=1}^N V_j (\mathbf{x}_j - \mathbf{x}_i)^m \nabla_i^n W_{ij} \right]^{-1}$  being the corrected matrix and  $m$  and  $n$  being the coordinate directions with repeated indices implying summation;  $\mathcal{D}^{mn} = 4 \frac{r_{ji}^m r_{ji}^n}{|r_{ji}|^2} - \delta^{mn}$  with  $\delta^{mn}$  being the Kronecker delta function;  $\tilde{F}_{ij} = \frac{r_{ji}^m}{|r_{ji}|^2} \cdot \hat{\nabla}_i^m W_{ij}$  is the scalar part of the normalised kernel gradient with  $\mathbf{r}_{ji} = \mathbf{x}_j - \mathbf{x}_i$  being the distance vector.

Several popular kernel functions have been derived in the literature [15,83]. Among these approaches, the cubic spline kernel function is considered in this paper:

$$W(q, h_{sml}) = \alpha_d \begin{cases} \frac{2}{3} - q^2 + \frac{1}{3}q^3 & 0 \leq q < 1 \\ \frac{1}{6}(2 - q)^3 & 1 \leq q < 2 \\ 0 & q \geq 2 \end{cases} \quad (54)$$

where  $\alpha_d = [1/h, 15/7\pi h^2, 3/2\pi h^3]$  is the dimensional normalising factor for one, two and three dimensions, respectively;  $q = |\mathbf{x}_i - \mathbf{x}_j|/h_{sml}$  is the normalised distance of a pair of particles; and  $h_{sml} = 1.2dx$  defined the smoothed length with  $dx$  being the initial distance between particles.

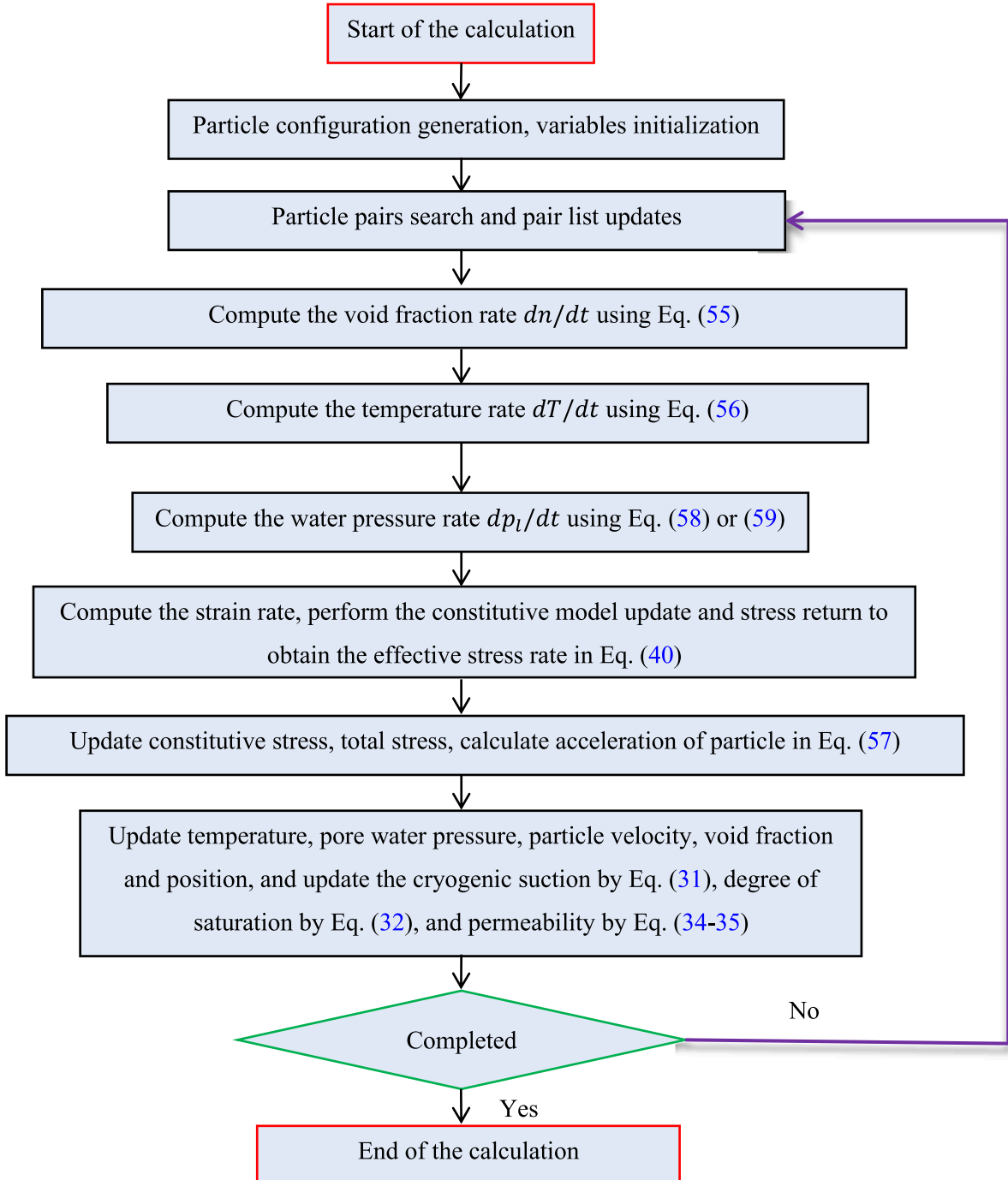
#### 4.2. SPH discretisation of the governing equations

To solve the coupled THM governing equations using SPH, one needs to convert these equations into SPH approximation forms. Simply, by applying the first derivative approximation (50) and the second derivative approximation (51) to the divergence terms, the following discretised forms of the governing equations in the fully coupled THM framework can be obtained:

Mass balance equation of the solid phase:

##### Algorithm 1

Implementation flowchart of the proposed THM-SPH framework.



$$\frac{dn_i}{dt} = \sum_{j=1}^N V_j (1 - n_j) \mathbf{v}_{ji}^s \cdot \hat{\nabla}_i \mathbf{W}_{ij} \quad (55)$$

Energy balance equation:

$$\left( \frac{dT}{dt} \right)_i = \frac{1}{(\rho c)_{eff} + n L_f T_i} \left[ -(\rho c)_{adv} \mathbf{W}_{is} \cdot \nabla T - \nabla \cdot (\lambda_{eff} \nabla T) \right] = \frac{1}{(\rho c)_{eff} + n L_f T_i} \left[ -(\rho c)_{adv} \mathbf{W}_{is} \cdot \sum_{j=1}^N V_j T_{ji} \hat{\nabla}_i \mathbf{W}_{ij} + \sum_{j=1}^N V_j T_{ji} \mathcal{D}^{mn} \tilde{F}_{ij} - \frac{\partial T}{\partial r^{m'}} \sum_{j=1}^N V_j T_{ji}^{m'} \mathcal{D}^{mn} \tilde{F}_{ij} \right] \quad (56)$$

Momentum balance equation of the entire mixture:

$$\left( \frac{d\mathbf{v}_s}{dt} \right)_i = \sum_{j=1}^N V_j \left( \frac{\boldsymbol{\sigma}_i + \boldsymbol{\sigma}_j}{\rho_i^t} \right) \cdot \nabla_i \mathbf{W}_{ij} + \mathbf{b} \quad (57)$$

Flow equation of water phase at frozen state:

$$\left( \frac{dp_l}{dt} \right)_i = \frac{1}{[n(1 - \eta)C_i + C_s]} \left\{ -[S_r + S_i \eta] \sum_{j=1}^N V_j \mathbf{v}_{ji}^i \cdot \hat{\nabla}_i \mathbf{W}_{ij} - n(1 - \eta) T_i \frac{dT}{dt} + \nabla \cdot \sum_{j=1}^N V_j \bar{k}_{mn}^{ji} H_{ji} \mathcal{D}^{mn} \tilde{F}_{ij} - k_i^{mn} \frac{\partial H}{\partial r^{m'}} \sum_{j=1}^N V_j T_{ji}^{m'} \mathcal{D}^{mn} \tilde{F}_{ij} \right\} \quad (58)$$

Flow equation of water phase at unfrozen state:

$$\frac{dp_l}{dt}_i = \frac{1}{C_s} \left\{ \sum_{j=1}^N V_j \bar{k}_{mn}^{ji} H_{ji} \mathcal{D}^{mn} \tilde{F}_{ij} - k_i^{mn} \frac{\partial H_i}{\partial r^{m'}} \sum_{j=1}^N V_j T_{ji}^{m'} \mathcal{D}^{mn} \tilde{F}_{ij} - \sum_{j=1}^N V_j \mathbf{v}_{ji}^s \cdot \hat{\nabla}_i \mathbf{W}_{ij} + \frac{1}{g} \sum_{j=1}^N V_j \bar{k}_{mn}^{ji} \left( \frac{d\mathbf{v}_{ji}^s}{dt} \right) \cdot \hat{\nabla}_i \mathbf{W}_{ij} \right\} \quad (59)$$

Eq. (55) is the mass balance equation of the solid phase in terms of porosity change rate,  $\mathbf{v}_{ji}^s$  is the velocity difference between two particles. Once the porosity of the soil skeleton is determined from Eq. (55), the change of saturated permeability and degree of saturation can be updated.  $T_i = dS_r/dT$  is the slope of the SFWC at temperature  $T$  in energy balance formulation (56). Eq. (57) is the momentum equation, and  $\rho^t$  is the total density of particle  $i$ , which is a function of the degree of saturation over time;  $\boldsymbol{\sigma}$  is the total Cauchy stress tensor. Eqs. (58) and (59) are the flow equations under frozen and unfrozen state, respectively.  $H_{ji}$  is the total head difference between particle  $i$  and  $j$ . These key governing equations are summarised in Algorithm 1, presented within a flowchart that outlines the step-by-step integration process.

#### 4.3. Time integration

The standard Leap-Frog (LF) algorithm is used to integrate the SPH approximation equations developed in the previous section. To this end, the state variables ( $Y$ ), including porosity ( $n$ ), temperature ( $T$ ), solid-phase stress ( $\boldsymbol{\sigma}^*$ ) and velocity ( $\mathbf{v}$ ), are updated at mid-step in time, while the displacement vector is updated at the full-time step as follows:

$$\mathbf{Y}_{t+\Delta t/2} = \mathbf{Y}_{t-\Delta t/2} + \Delta t \left( \frac{d\mathbf{Y}}{dt} \right)_t \quad (60)$$

$$\mathbf{x}_{t+\Delta t}^s = \mathbf{x}_t^s + \Delta t \cdot (\mathbf{v}^s)_{t+\Delta t/2} \quad (61)$$

The stability of the LF time integration scheme is maintained by the Courant-Friedrichs-Lewy (CFL) condition. The overall timestep size is restricted by:

$$\Delta t \leq \min(\Delta t_s, \Delta t_l, \Delta t_T) \quad (62)$$

where  $\Delta t_s$ ,  $\Delta t_l$  and  $\Delta t_T$  are the time step size determined from the solid phase, water phase and thermal conduction. The time step size for the solid phase that satisfied the CFL condition is given as:

$$\Delta t_s \leq C_{CFL} \frac{h_{sml}}{c_{sp}} \quad (63)$$

where  $C_{CFL}$  is a constant, which is taken to be 0.1 throughout this paper;  $c_{sp} = \sqrt{E_s/\rho_s}$  is the speed of sound in the solid phase with  $E_s$

being Young's modulus of the solid phase.

As for the hydraulic calculation of the seepage flow, the timestep is restricted by the following condition:

$$\Delta t_l \leq C_{CFL} \frac{\tilde{C}_s h_{sml}^2}{k^{sat}} \quad (64)$$

The last term of the time step size for thermal conduction is given as:

$$\Delta t_T \leq C_{CFL} \frac{\tilde{C}_T h_{sml}^2}{\lambda_{eff}} \quad (65)$$

where  $\tilde{C}_T = (\rho c)_{eff} + nL_f T_i$ . It is noted that the time step size for the heat conduction problem can usually be very large, thus, the time increment for the coupled THM analysis is mainly defined by the solid phase or the water phase. It is noted here that within the applied LF algorithm, the governing equations summarised in the Algorithm 1 are solved monolithically for each time step, and no iteration is involved.

#### 4.4. SPH stabilisation techniques

##### 4.4.1. Global viscosity damping

The integration of the fully dynamic form of the momentum equation for the particle motions could lead to free vibration to SPH particles due to inertial force or sudden external loads in non-dissipative materials (or elastic materials) [28,32]. To remove this oscillation so as to obtain a smooth and accurate stress/pressure field, the widely used global viscous damping is applied for stabilisation in the THM-SPH framework, taking the following forms:

$$\mathbf{F}_d = -c_d \cdot \mathbf{v}_s \quad (66)$$

where  $c_d$  stands for a damping coefficient, calculated from solid properties following the approach proposed by Bui et al. (2013) [32] as follows:

$$c_d = \eta_d \sqrt{E_s / (\rho_s h_{sml}^2)} \quad (67)$$

where  $\eta_d$  denotes a non-dimensional damping coefficient, of which the value is recommended to range from 0.02 to 0.1 by Bui et al. (2013) [32]. After the employment of the global viscous damping force, the final momentum equation is given as follows:

$$\left( \frac{d\mathbf{v}_s}{dt} \right)_i = \sum_{j=1}^N V_j \left( \frac{\sigma_i + \sigma_j}{\rho_i^t} + \mathbf{C}_{ij} \right) \nabla_i \mathbf{W}_{ij} + \mathbf{F}_d + \mathbf{b} \quad (68)$$

where  $\rho^t$  is the total density of particle  $i$ , which varies over time with the degree of saturation; and  $\mathbf{C}_{ij}$  is a stabilisation term consisting of the artificial viscosity and artificial stress commonly adopted in SPH to remove stress fluctuation and tensile instability, respectively [24,28,30,32]. The specific details of these techniques are not repeated here. It is also noted that the global viscosity damping force is only applied to non-dissipative or elastic materials.

##### 4.4.2. Stabilisation of pore-water pressure

Similar to the coupled flow-large deformation analysis on low-permeable soils [17], the non-physical spatial oscillation in the fluid pressure field is also found in the currently coupled THM-SPH framework. This issue is attributed to the incompressible or nearly incompressible ice and liquid in the frozen mixture, where the very stiff response of these components in the mixture causes pore-water pressure fluctuation [84,85]. In the fully dynamic formulations, even small particle displacements can cause significant pore pressure fluctuations due to the strong coupling effect. This instability is further amplified under dynamic large deformation conditions, where particle oscillations are more pronounced. To address this issue, the well-known Shepard regularisation technique is considered herein, which takes:

$$p_l^i = \frac{\sum_{j=1}^N V_j W_{ij} p_l^j}{\sum_{j=1}^N V_j W_{ij}} \quad (69)$$

Eq. (69) is applied to each particle after every  $m$  computational cycle, which may vary from different applications [28,52]. In this study,  $m = 1000$  is adopted, and it is only applied to the modelling of the thawing-induced slope failure problem.

##### 4.4.3. Negative pore water pressure stabilisation

When modelling large deformation, as the soil is undergoing slight plastic dilation, Eq. (59) can overestimate the increased negative excess pore-water pressure, which can subsequently lead to tensile stress that further causes the well-known tensile instability problems in SPH [17]. To tackle this issue, a stabilisation equation proposed in our previous work [17] is also adopted here:

$$\frac{dp_l}{dt} = \begin{cases} \frac{1}{C_s^f} \left\{ \sum_{j=1}^N V_j \bar{K}_{mn}^{ji} H_{ji} \mathcal{D}^{mn} \tilde{F}_{ij} - \sum_{j=1}^N V_j \mathbf{v}_{ji}^s \cdot \hat{\nabla}_i W_{ij} + A \right\} & p_l^t > 0 \\ \frac{1}{C_s^f + C_s^u} \left\{ \sum_{j=1}^N V_j \bar{K}_{mn}^{ji} H_{ji} \mathcal{D}^{mn} \tilde{F}_{ij} - \sum_{j=1}^N V_j \mathbf{v}_{ji}^s \cdot \hat{\nabla}_i W_{ij} + A \right\} & p_l^t < 0 \end{cases} \quad (70)$$

where the notation  $A = -k_{mn}^{ij} \frac{\partial p_l}{\partial r^m} \sum_{j=1}^N V_j \mathbf{r}_{ji}^{m'} \mathcal{D}^{mn} \tilde{F}_{ij} + \frac{1}{g} \sum_{j=1}^N V_j \bar{K}_{mn}^{ji} \left( \frac{dv_{ji}^s}{dt} \right) \cdot \hat{\nabla}_i W_{ij}$  is used to simplify the expression of the equations.  $C_s^u$  is the stabilisation coefficient governing the increasing rate of the negative pore-water pressure [17]. In this study,  $C_s^u = 4 \times 10^{-6} \text{ Pa}^{-1}$  is adopted in all simulations involving large deformation.

#### 4.4.4. Stabilisation technique for convection-dominated problems

Solving the energy balance equation, Eq. (33), in frozen porous media involves a hybrid convection-diffusion formulation, which could lead to numerical instability when convection becomes dominant. This issue is quantified by the Peclet number, which is a function of the convection and diffusion coefficients and the mesh size (i.e.,  $P_e = wdx/D$ , where  $w$  is the convection coefficient and  $D$  being the diffusion coefficient). When the  $w \gg D$ , the problem becomes convection-dominated, causing the diffusion term to nearly diminish in heat conduction. Under the Dirichlet boundary condition, this can result in so-called downstream boundary conditions [86], where the sharp temperature gradient becomes difficult to solve numerically, leading to non-physical spatial oscillations (also known as ‘wiggles’). Such instability has been reported frequently in several numerical methods, including FEM and MPM [19,86–88]. Special treatments, such as mesh refinement or advanced integration schemes like the Petrov-Galerkin weighted residual method [86, 87], are often required.

This issue is not an exception in SPH, as highlighted in our previous work on solving the concentration transport equation in the five-phase computational framework for internal erosion [52]. A concentration regularisation technique was introduced to obtain a stable solution for the pure-convection problems [52]. In this study, an alternative stabilization approach is proposed to solve the problem. This approach is inspired by the ‘density diffusion approach’, originally proposed by Antuono and his co-workers [89], for the free-surface flows problem. The corresponding diffusive term for temperature is given as follows:

$$D_T = \delta h_{\text{smal}} \sum_{j=1}^N V_j \Psi_{ij} \cdot \hat{\nabla}_i W_{ij} \quad (71)$$

where  $\Psi_{ij}$  is calculated as follows:

$$\Psi_{ij} = 2(T_j - T_i) \frac{r_{ji}}{|r_{ji}|^2} - [\langle \nabla T_i^L \rangle + \langle \nabla T_j^L \rangle] \quad (72)$$

$$\langle \nabla T_i^L \rangle = \sum_{j=1}^N V_j (T_j - T_i) \hat{\nabla}_i W_{ij} \quad (73)$$

where  $\langle \nabla T_i^L \rangle$  is the renormalised temperature gradient, with  $\langle \cdot \rangle$  being the Macaulay brackets.  $\delta$  is an adaptive parameter determining the amount of artificial heat diffusion added to the convection-diffusion process. In this study, it is defined as follows:

$$\delta = \delta_0 * \left[ \coth|P_e| - \frac{1}{P_e} \right] \quad (74)$$

In the above formulation,  $\delta$  increases as the Peclet number increases, and it converges to the maximum value  $\delta_0$ , which is found to be 0.1 in this study. This temperature diffusion plays a key role in removing the spatial oscillation in the formulation of temperature, ensuring smooth heat conduction in a convection-dominated problem.

Notably, the diffusion term vanishes when the temperature field is constant or uniformly distributed, ensuring it serves exactly to stabilise the numerical solutions. Moreover, for small Peclet numbers, the diffusion term itself in the governing equation can ensure stability, making additional stabilisation unnecessary. This situation is covered by Eq. (74), where  $\delta$  remains negligible when the convection effect is weak.

For highly convective problems, the governing equation for temperature now becomes:

$$\frac{dT}{dt} = \frac{1}{(\rho c)_{\text{eff}} + n L_f T_i} \left[ -(\rho c)_{\text{adv}} \mathbf{w}_{ls} \cdot \sum_{j=1}^N V_j T_{ji} \hat{\nabla}_i W_{ij} + \sum_{j=1}^N V_j T_{ji} \mathcal{D}^{mn} \tilde{F}_{ij} - \frac{\partial T}{\partial r^m} \sum_{j=1}^N V_j \mathbf{r}_{ji}^{m'} \mathcal{D}^{mn} \tilde{F}_{ij} + D_T \right] \quad (75)$$

Verifications of the proposed scheme will be given in Section 5.

#### 4.4.5. Alternative TPI integration scheme for the flow equation

Solving pore water pressure using the explicit integration scheme (Eqs. (58) and (59)) can be computationally demanding, particularly for highly permeable soils. In this case, the Courant-Friedrichs-Lewy (CFL) condition (Eq. (64)) imposes a small time step,



significantly increasing computational costs [17].

To overcome this issue, the recently proposed Three Point Integration (TPI) method is also considered in this study. Following the same derivation process in our previous work [17], which is not repeated here, the governing Eq. (21) in the TPI integration scheme can be expressed as:

$$p_{li}^{t+1} = \frac{B_{ij} + \sum_{j=1}^N A_{ij} p_{lj}^{t+\alpha} + C_j p_{li}^{t+\alpha} / \Delta t}{\sum_{j=1}^N A_{ij} + C_j / \Delta t} \quad (76)$$

where

$$\begin{aligned} A_{ij} &= V_j \bar{k}_{mn}^{ji} \mathcal{D}^{mn} \tilde{F}_{ij} \\ B_{ij} &= -\gamma_l [S_r + S_l \eta] \nabla \cdot \mathbf{v}_s + \gamma_l \nabla \cdot [\mathbf{k}_l \nabla (z)]_i - E_j \\ C_j &= -\gamma_l n(\eta - 1) C_i \\ E_i &= k_i^{mn} \frac{\partial p_{li}}{\partial r^{m'}} \sum_{j=1}^N V_j r_{ji}^{m'} \mathcal{D}^{mn} \tilde{F}_{ij} \end{aligned} \quad (77)$$

For a fully saturated unfrozen condition, Eq. (76) reduces to:

$$p_{li}^{t+1} = \frac{B_{ij} + \sum_{j=1}^N A_{ij} p_{lj}^{t+\alpha}}{\sum_{j=1}^N A_{ij}} \quad (78)$$

where  $p_{lj}^{t+\alpha} = p_{lj}^t + \alpha(p_{lj}^t - p_{lj}^{t-1})$  is an “intermediate” pressure evaluated from the last time step [17].  $\alpha$  is suggested as 0.5 in all of these simulations [17].

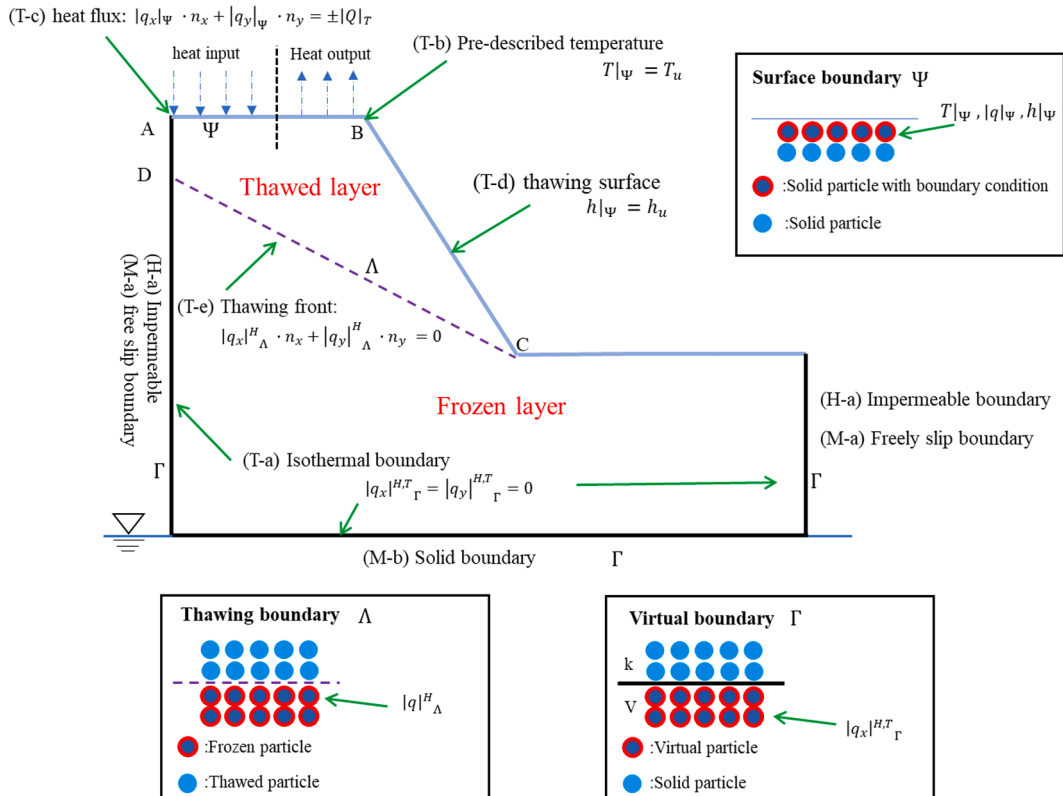


Fig. 8. Diagram of the common thermal boundary conditions in SPH simulations.

#### 4.5. Thermal boundary implementations

A well-defined boundary condition is essential for modelling the boundary value problems involving the fully coupled THM processing and large deformation in SPH. Given that this study represents the first attempt to address such problems using the single-layer SPH method, common boundary conditions required for THM problems are discussed, as illustrated in Fig. 8. Only the implementation of thermal boundary conditions is given here; details of the rest of the mechanical and hydraulic boundary conditions can be found in our previous works [15,18,24].

##### T-a. Isothermal boundary

Similar to the seepage flow modelling, virtual particles are used to model the isothermal boundary  $\Gamma$  (See virtual boundary in Fig. 8), where no heat flux can occur over the isothermal boundary:

$$|q_x|_{\Gamma}^T = |q_y|_{\Gamma}^T = 0 \quad (79)$$

where  $|q_x|_{\Gamma}^T$  and  $|q_y|_{\Gamma}^T$  indicate the heat flux over  $x$  and  $y$  direction with  $T$  denoting the thermal boundary. To model this boundary condition, the same thermal properties of the boundary particles are enforced as follows:

$$T^v = T^k, \lambda_{eff}^v = \lambda_{eff}^k \text{ and } (\rho c)_{eff}^v = (\rho c)_{eff}^k \quad (80)$$

where the subscript “v” denotes boundary particles within the support domain of the real solid particle “k”. Eq. (80) ensures that all the virtual boundary particles have a zero thermal gradient, thus guaranteeing zero heat flux crossing the boundary.

##### T-b. Prescribed temperature boundary

This type of boundary commonly occurs at the ground surface  $\Psi$ , where external temperature change induces soil thawing or freezing. To model such a condition, the Dirichlet boundary condition is required and involves imposing a constant temperature to the surface particle as follows:

$$T|_{\Psi} = T_u \quad (81)$$

where  $T_u$  is the external temperature. Surface particles can be detected by the following conditions:

$$\Psi_{surf} = \sum_{j=1}^N W_{ij} V_j < \eta_{lim} \quad (82)$$

where  $\eta_{lim}$  is the threshold value less than one. In this study,  $\eta_{lim}$  is selected as 0.84, which can effectively identify surface particles and prevent inner particles from being mistakenly identified when there is plastic dilation in most cases. It is noted that the threshold used in the surface detection algorithm in Eq. (82) must be carefully selected to avoid misidentifying inner particles as free-surface particles, particularly under conditions of extremely large deformation. To completely eliminate this issue, more advanced surface detection algorithms [90] should be considered. However, the implementation of such methods is beyond the scope of this study.

##### T-c. Heat flux boundary

Another commonly encountered surface boundary in THM problems is the heat flux boundary, which is also known as the Neumann boundary condition. In this case, a pre-described heat flux takes the form:

$$|q_x|_{\Psi}^T \cdot n_x + |q_y|_{\Psi}^T \cdot n_y = \pm |Q|^T \quad (83)$$

where  $|Q|^T$  is the source/sink term with the positive sign denoting heat input and the negative sign for heat output;  $n_x$  and  $n_y$  are the normal vectors.

##### T-d. Thawing surface boundary

In a thawing test, frozen soil starts to thaw from the ground surface, where ice melts into water, generating significant excess melted water in the thawed zone. Due to the low permeability of the underlying frozen ground, the infiltration capability of the soil is highly restricted, limiting the infiltration of the free unfrozen water. As a result, melted water may accumulate and flow over the ground surface  $\Psi$ , leading to a “ponding” condition on the surface particle. This boundary condition can be imposed in SPH as follows:

$$h|_{\Psi} = h_u \quad (84)$$

where  $h|_{\Psi}$  is the water pressure head and  $h_u$  is determined by the infiltration capacity of the soil, which can be calibrated via an

experimental study. In this study, for the thawing surface, a value of  $-0.1$  m is selected. Under this condition, a “ponding” water head is applied to surface particles when it is unfrozen, together with either heat flux or constant temperature boundary when modelling the thawing process.

### T-e. Thawing front boundary

During thawing, an impermeable interface  $\Lambda$  may form at the thawing front (see line DC in Fig. 8) due to the extremely low permeability of the underlying frozen layer. Melted water cannot infiltrate the frozen ground, thus accumulating at the freezing-thawing interface and generating high excess pore water pressure. This accumulated water is well known as the major contributor to the cryogenic landslides [1]. To capture this effect, a thin impermeable interface condition [18] is imposed at the thawing front by preventing the water flux across the freezing-thawing interface. A straightforward way is to ignore the hydraulic interaction when dealing with the particle pairs crossing the interface [18].

For fully-coupled THM modellings, mechanical boundaries (e.g., free-slip and solid boundaries) and hydraulic boundaries (e.g., impermeable boundary) are still required. Readers are referred to our previous works [15,18,24] for detailed implementation, which is not repeated here.

## 5. Model verifications

### 5.1. Verification of the constitutive model implementation

Before implementing the constitutive model into the fully coupled THM-SPH framework for thawing-induced slope failure simulations, a simple shear test is conducted to verify the performance and accuracy. The stress loading paths, corresponding to different cryogenic suctions (i.e.,  $s_{1,2,3} = 1.2, 2.4, 4.8$  MPa and saturations  $S_{r,1,2,3} = 0.75, 0.55, 0.25$ ), are given in Fig. 9(a).

First, the CASM-F model is programmed in MATLAB for a single-element test to simulate stress-strain response under simple shear conditions. The model is then incorporated in our in-house SPH code for the same loading conditions, with the geometry setup illustrated in Fig. 9(b) [15]. In this test, 900 particles are placed in a cubic box, with the central region representing a soil element. The material properties for this test are given in Table 3.

The soil sample is initially confined under a pressure of 150 kPa. To facilitate the shearing, an initial velocity field ( $v_{xi} = v_0 y_i, v_{yi} =$

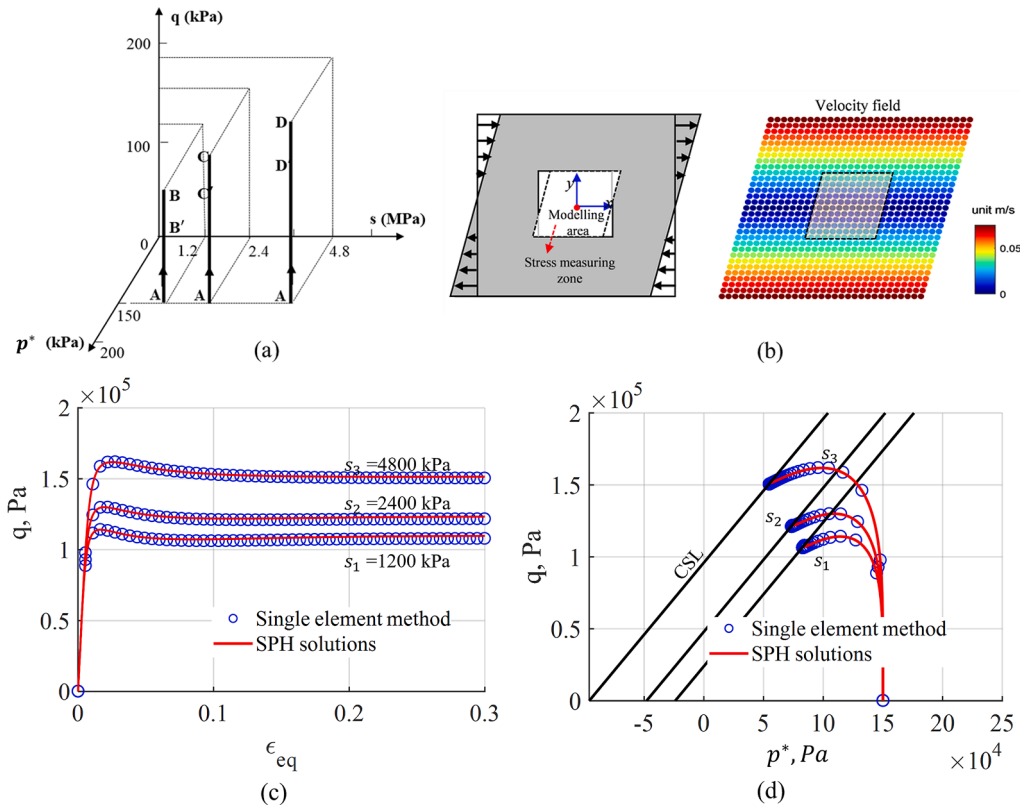


**Fig. 9.** Verification of the SPH implementation of the CASM-F model. (a) Loading paths; (b) Setting of simple shear test in SPH; (c) Predicted stress-strain relations; (d) Predicted stress loading path.

**Table 3**

Material and model parameters for the constitutive modelling.

	Parameters	Symbol	Value
Mechanical properties	Compression index	$\lambda_0$	0.20
	Swelling index	$\kappa$	0.02
	SI parameter	$\kappa_s$	0.01
	Freezing bring-up stiffness (MPa)	$K_i$	5
	Poisson's ratio	$\nu$	0.33
	Slope of CSL	$M$	1.0
	Bring-up cohesion parameter	$k_t$	0.02
	Segregation threshold (MPa)	$s_0$	1.2
	LC stiffness coefficient	$r$	0.75
	LC stiffness coefficient ( $\text{Pa}^{-1}$ )	$\beta$	$0.0125 \times 10^{-6}$
	Initial pre-consolidation pressure (MPa)	$p_0^*$	0.15
	Reference pressure (MPa)	$p_r$	0.1
	Constitutive parameter	$r_c$	1.75
	Constitutive parameter	$n_c$	4.5
	Initial void ratio	$e_0$	1.21
	Subloading parameter	$R_0$	15

0, with  $v_0 = 0.75 \text{ m/s}$  is assigned to all particles, of which the velocity of the boundary particle is kept unchanged, whereas the central particles are allowed to move freely. The predicted stress-strain responses from the SPH method and the MATLAB single-element test are compared in Fig. 9(c), with the stress paths and critical state lines (CSLs) shown in Fig. 9(d). The CASM-F model captures well the shear strength variation against different cryogenic suctions, suggesting higher peak shear strength at higher cryogenic suction, which is consistent with the increased strength of frozen soil at lower temperatures. The SPH predictions agree well with the single-element results, suggesting a correct implementation in SPH.

## 5.2. Heat conduction verification

### 5.2.1. One-dimensional heat transfer problem – A pure diffusion problem

The verification of the coupled THM-SPH framework begins with the one-dimensional pure heat conduction problem. To simplify the analysis, the rigid media is considered, and thus, the governing partial differential Eq. (33) reduces to:

$$((\rho c)_{\text{eff}}) \frac{dT}{dt} + \nabla \cdot (\lambda_{\text{eff}} \nabla T) = 0 \quad (85)$$

Fig. 10 shows the problem setup. This benchmark test was first introduced by Cleary & Monaghan (1999) [77] to verify their SPH approximation formulation for the second-order derivation. A one-meter slab with its left half being initially at  $0^\circ\text{C}$  and the right half being at  $1^\circ\text{C}$ , is considered. The material properties are identical to Cleary & Monaghan (1999) [77] for a comparison purpose:  $\rho = 1000 \text{ kg/m}^3$ ,  $c_{\text{eff}} = 1 \text{ J/(kg} \cdot \text{K)}$ . Two scenarios for the heat conductivity are considered:  $\lambda_{\text{eff}} = 1 \text{ W/(m} \cdot \text{K)}$  and  $\lambda_{\text{eff}} = \exp(\kappa T) \text{ W/(m} \cdot \text{K)}$ .

Fig. 11 shows the temperature profile across the slab at time intervals, showing strong agreement between the THM-SPH predictions and the reference results [77]. In the first case, heat gradually transfers from the hot end to the cool end, displaying a central symmetric shape of curves due to constant conductivity (Fig. 11(a)). In the temperature-dependent coefficient case, the higher conductivity at the hot end enhances heat flux toward the cold end, leading to rapid heating. Overall, the proposed framework predicts the heat conduction problem well.

### 5.2.2. One-dimensional convection-diffusion heat transfer problem

The one-dimensional convection-diffusion heat transfer problem is then considered to further verify the coupled THM-SPH framework for the transient heat transfer in porous media subjected to a seepage flow. To simplify the analysis, the porous media is again assumed rigid, and seepage flow is explicitly imposed rather than solving the entire transient seepage equation. Under this consideration, the governing Eq. (33) reduces to:

$$((\rho c)_{\text{eff}}) \frac{dT}{dt} + (\rho c)_{\text{adv}} \mathbf{w}_{\text{is}} \cdot \nabla T + \nabla \cdot (\lambda_{\text{eff}} \nabla T) = 0 \quad (86)$$

The resulting equation represents a typical convection-diffusion heat transfer problem, where numerical solutions might encounter instability issues, particularly at high seepage velocity associated with a large Peclet number. In this section, we will demonstrate that

**Fig. 10.** Geometry for the heat conduction problem.

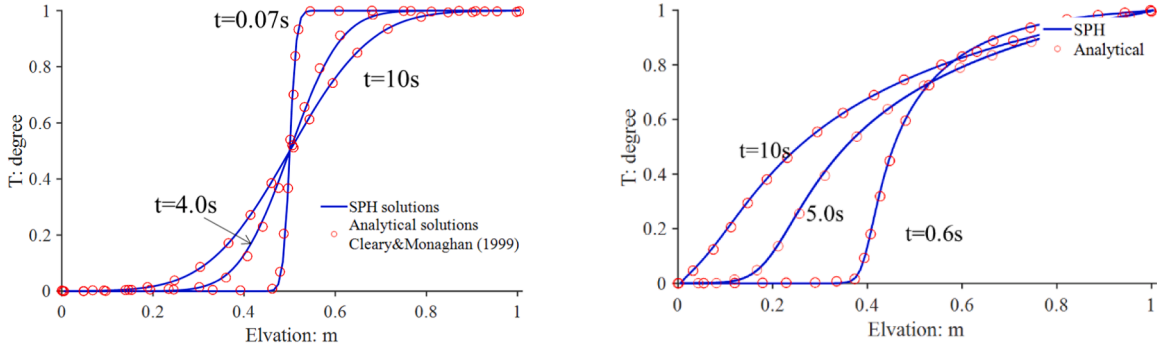


Fig. 11. Temperature profile across the slab at different time intervals. (a)  $\lambda_{eff} = 1 \text{ W/(m} \cdot \text{K)}$ ; (b)  $\lambda_{eff} = \exp(\kappa T) \text{ W/(m} \cdot \text{K)}$ ,  $\kappa = 4$ .

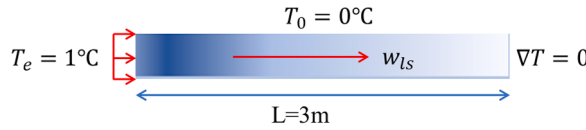


Fig. 12. Geometry for the coupled advection-diffusion heat transfer.

the proposed THM-SPH framework with the stabilisation technique of temperature diffusion can effectively resolve this issue.

Fig. 12 illustrates the problem setup, of which the heat conduction is solved using the proposed THM-SPH framework. A homogenous slab, initially at  $0^\circ\text{C}$ , is subjected to a constant rightward seepage flow field  $\mathbf{w}_{ls}$ . A Dirichlet boundary condition is applied at the left end to maintain a constant temperature of  $1^\circ\text{C}$ , enforcing a thermal gradient. The slab is modelled as a rigid solid consisting of 600 particles with a spacing distance of 0.03 m. The time step is determined from the condition (65) for thermal conduction problems.

The following material properties are adopted:  $\rho = 1000 \text{ kg/m}^3$ ,  $c_{eff} = 0.001 \text{ J/(kg} \cdot \text{K)}$ ,  $c_{adv} = 0.01 \text{ J/(kg} \cdot \text{K)}$ ,  $\lambda_{eff} = 0.05 \text{ W/(m} \cdot \text{K)}$ . Three different seepage flow velocity  $\mathbf{w}_{ls}$  of 0.0467 m/s, 0.083 m/s and 0.20 m/s are considered, corresponding to the Peclet numbers being around 0.28, 0.5. and 1.20, respectively. It is noted here that these field variables may not represent any field scenario, and they are designed for demonstration purposes. For this problem, the analytical solution for the temperature profile can be given as follows [91]:

$$T(x, t) = \frac{1}{2}T_e \text{erfc} \left[ \frac{R'x - wt}{2(DR't)^{0.5}} \right] + \frac{1}{2} \exp(wx/D) \text{erfc} \left[ \frac{R'x + wt}{2(DR', t)^{0.5}} \right] + \frac{1}{2}T_e \left[ 2 + \frac{w(2L - x)}{D} + \frac{w^2t}{DR'} \right] \exp(wL/D) \text{erfc} \left[ \frac{R'(2L - x) + wt}{2(DR't)^{0.5}} \right] - T_e \left( \frac{w^2t}{\pi DR'} \right)^{0.5} \exp \left[ \frac{wL}{D} - \frac{R'}{4Dt} \left( 2L - x + \frac{wt}{R'} \right)^2 \right] \quad (87)$$

where  $R' = ((\rho c)_{eff})$  is the effective heat capacity,  $w = (\rho c)_{adv} \mathbf{w}_{ls}$  stands for the convection coefficient and  $D = \lambda_{eff}$  indicates the

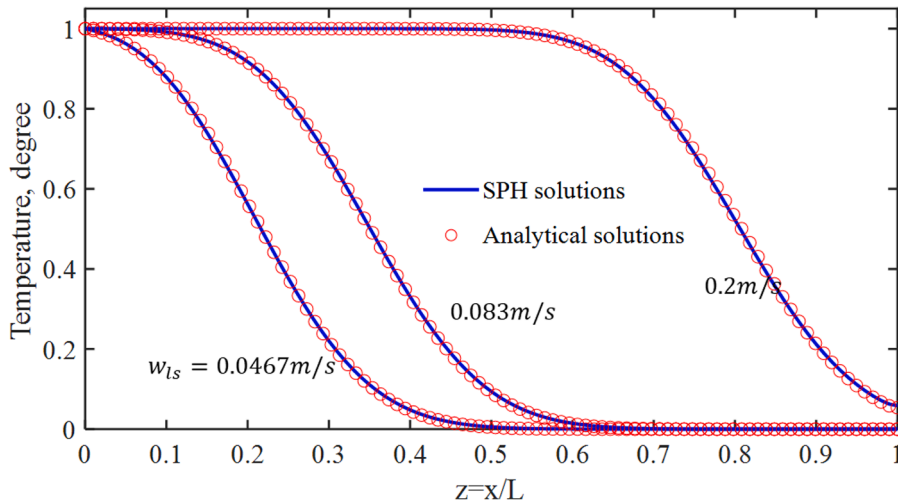


Fig. 13. Temperature profile of the coupled advection-diffusion heat transfer problem at three different seepage flow velocities when  $t = 1.2 \text{ s}$ .

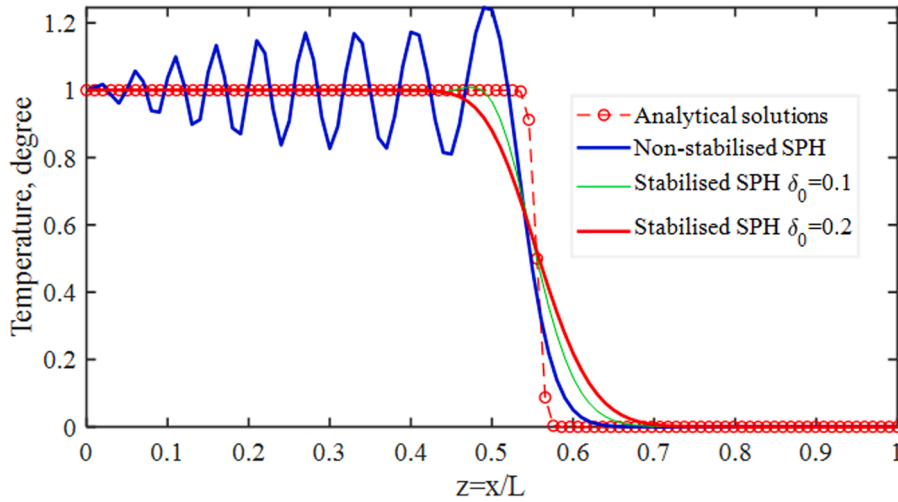


Fig. 14. Temperature profile convection-dominated heat transfer problem with  $Pe=200$  when  $t = 0.0050$  s.

diffusion coefficient.

Fig. 13 shows the temperature profile in the slab subjected to three different seepage velocities, where the predicted temperature profiles match very well with the analytical solutions. As the seepage velocity increases, heat conduction accelerates due to enhanced heat advection.

Next, to demonstrate the performance of the proposed temperature diffusion scheme in convection-dominated problems, the applied seepage flow  $w_s$  is increased to 33.3m/s, corresponding to an extreme Peclet number of 200. The results are given in Fig. 14. In the non-stabilised solution, a high unphysical oscillation is observed in the upstream region of the heat wave propagation path. On the contrary, the proposed temperature diffusion approach smooths out this oscillation, producing a nearly oscillation-free temperature profile that is close to the analytical solution, with only minor oscillation being observed in the heat front. This minor fluctuation can be further reduced by increasing the diffusion coefficient  $\delta_0$  to 0.2, but at a cost that more diffusion is introduced to the solution. These results highlight that careful consideration is required to balance the accuracy and instability in the solution when applying the diffusion scheme to convection-dominated problems. Nevertheless, the proposed method offers an effective way to deal with the non-physical oscillation in the convection-diffusion problem with high Peclet numbers.

### 5.3. One-dimension heat transfer-induced soil freezing modelling

In this section, a one-dimensional freezing test of a hypothesis soil column is examined to evaluate the capacity of the proposed THM-SPH framework. The problem was previously studied by Bekele et al. (2017) [58] using FEM, and part of the presented results will be used as a reference. The problem setup is illustrated in Fig. 15. The soil domain is 2 m in height and 0.2 m in width, modelled as

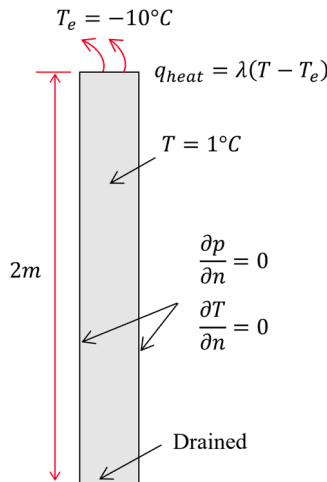


Fig. 15. The geometry and boundary condition for the one-dimension THM freezing problem (After Bekele et al., (2017) [58]).

**Table 4**

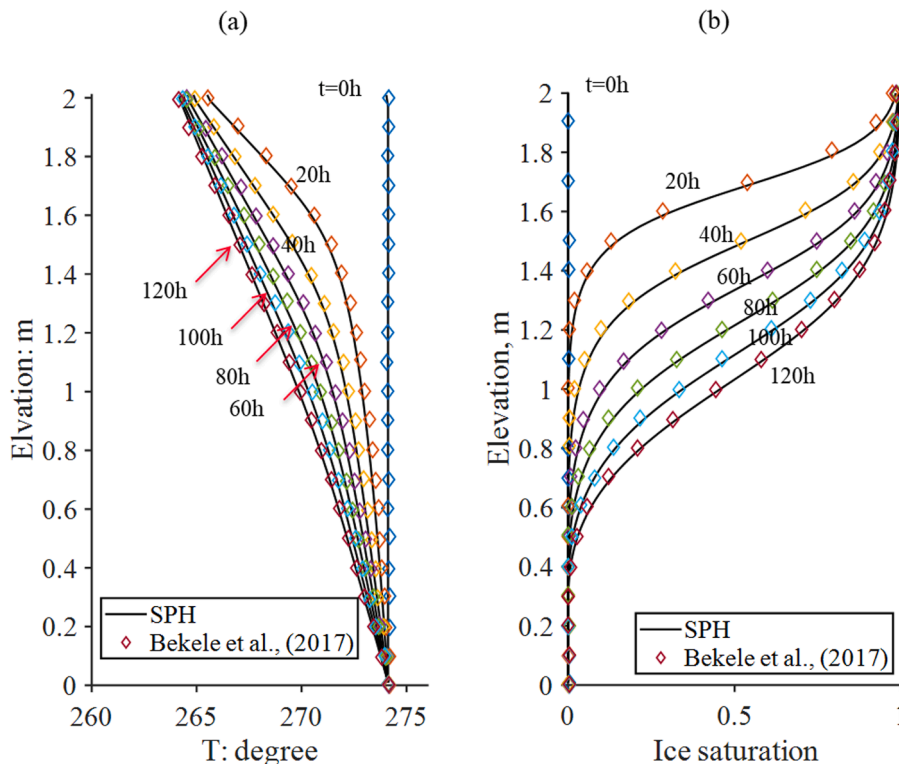
Material and model parameters for one-dimensional thaw consolidation (after Bekele et al., 2017) [58]).

	Parameters	Symbol	Value
Mass properties	Soil density ( $\text{kg/m}^3$ )	$\rho_s$	2650
	Ice density ( $\text{kg/m}^3$ )	$\rho_i$	910
	Water density ( $\text{kg/m}^3$ )	$\rho_l$	1000
Thermal properties	Initial porosity	$n_i$	0.44
	Freezing point ( $^{\circ}\text{C}$ )	$T_k$	1.0
	Heat conductivity of soil ( $\text{W/m/K}$ )	$\lambda_s$	1.5
	Heat conductivity of ice ( $\text{W/m/K}$ )	$\lambda_i$	2.20
	Heat conductivity of water ( $\text{W/m/K}$ )	$\lambda_l$	0.6
	Heat capacity of soil ( $\text{J/kg/K}$ )	$c_s$	800
	Heat capacity of ice ( $\text{J/kg/K}$ )	$c_i$	2095
	Heat capacity of water ( $\text{J/kg/K}$ )	$c_l$	4190
	Latent heat of fusion ( $\text{J/kg}$ )	$L_f$	$3.34 \times 10^5$
Hydraulic properties	Saturated permeability ( $\text{m/s}$ )	$k_s^{\text{sat}}$	$1 \times 10^{-8}$
	SFWC parameter ( $\text{Pa}^{-1}$ )	$g_a$	$0.1 \times 10^{-6}$
	SFWC parameter	$g_n$	2.5
	SFWC parameter	$g_c$	-8.0
	Kozeny-Carman coefficient	$C_k$	2

a homogeneous elastic material using 1000 particles with a spacing of 0.02 m. Table 4 provides the material properties, with the hydraulic conductivity being constant.

Initially, the material slab is at a uniform temperature of  $1^{\circ}\text{C}$ , and a cooling source is imposed on the top surface by setting the environment temperature to  $-10^{\circ}\text{C}$ . The bottom boundary is maintained at a constant temperature of  $1^{\circ}\text{C}$ , while the other boundaries remain isothermal. A hydrostatic pore water pressure is also assigned to the soil bar, with the bottom boundary being drained to supply water when the phase change occurs, while the other boundaries remain undrained. This example is designed to verify the capability of the model in capturing the formation of ice content during freezing, and it is noted here that the deformation is neglected. The time step size is 200 s.

Fig. 16 compares the results predicted by the proposed THM-SPH framework and those of Bekele et al. (2017) [58] over 120 h, demonstrating a good agreement between the two approaches. Initially, a sharp drop in the temperature is observed at the first 20 h due to a high-temperature gradient on the surface, as shown in Fig. 16(a). As cooling progresses, heat infiltration becomes slower and

**Fig. 16.** Profiles of (a) Temperature; (b) Ice saturation; (c) Pore water pressure (PWP) of the one-dimension THM freezing problem.



gradually transfers downwards until an equilibrium condition at 120 h.

As the temperature decreases below the freezing point, ice begins to form, as illustrated in the ice saturation curves in Fig. 16(b), where the predicted results match well with the FEM results by Bekele et al. (2017) [58]. Overall, the proposed THM-SPH framework effectively predicts the complex freezing process, including heat transfer and ice content development.

#### 5.4. Coupled THM process: a non-isothermal consolidation in the saturated soil column

To verify the proposed THM-SPH framework for fully coupled THM processes, the one-dimensional thermo-elastic consolidation analysis on a saturated soil column, first presented by Aboustit et al. (1985) [92], is considered in this section. The problem setup is illustrated in Fig. 17.

The fully saturated soil column is 7 m in height and 0.3 m in width, which is modelled using 840 particles with a spacing of 0.05 m. The soil column is initialised with a zero temperature, pore water pressure and stress. At the early stage of the analysis, a surcharge loading of 1 kPa is applied on the top surface, while all other boundaries remain undrained and isothermal. At this stage, the external load is entirely carried by the water, generating excess pore water pressure. After the loading stage, the top surface is assigned a zero pore pressure and a temperature of 50 °C, triggering the excess pore water pressure dissipation and heat infiltration. The evolution of temperature, pore water pressure and displacement are measured during the consolidation process and compared with the analytical solutions. It is noted that the advection heat transfer is disregarded for consistency with the work by Aboustit et al. (1985) [92] and other researchers [19] since the seepage flow is too insignificant to cause heat advection.

To ensure consistency with previous studies by Aboustit et al. (1985) [92] and Gao & Ghassemi (2020) [93], the same parameters are adopted. These include Young's modulus ( $E$ ) = 6 MPa, Poisson's ratio ( $\nu$ ) = 0.4, a constant saturated permeability ( $k_{sat}$ ) =  $4 \times 10^{-3}$  m/s, porosity ( $n$ ) = 0.2, a constant thermal conductivity of the soil mixture ( $\lambda_{eff}$ ) =  $863 \times 10^2$  W/m/K, matrix heat capacity ( $\rho c_{eff}$ ) =  $167.2 \times 10^3$  J/(m<sup>3</sup>K) corresponding to  $\rho_s = \rho_l = 1000$  kg/m<sup>3</sup>,  $c_l = c_s = 167.2$  J/kg/K, and the solid expansion coefficient =  $9 \times 10^{-7}$  / (Pa · K).

Fig. 18 compares the predicted temperature evolution at three monitoring locations by the proposed THM-SPH model with the results reported in the previous studies [92,93], using the dimensionless time factor defined by  $T_V = [k_{sat}E(1 - \nu)t] / [\gamma_l(1 - 2\nu)(1 + \nu)L^2]$ . Excellent agreements were achieved, suggesting the accuracy of the THM-SPH framework in capturing THM problems. The first thermal response is observed at the first measuring point at an elevation of  $Z = 5.6$  m, followed by  $Z = 4.2$  m, and  $Z = 1.4$  m. After a transient period, all measured values converge to 50 °C, corresponding to the applied boundary condition.

Fig. 19 compares the predicted displacement at the same measuring points, demonstrating excellent agreement with the reference solutions. Initially, the soil column experiences vertical settlement and reaches the maximum value at  $T_V \approx 1.88$ , as the excess pore water pressure dissipation is completed. After that, the thermal expansion begins to dominate, rebounding back the settlement curve in

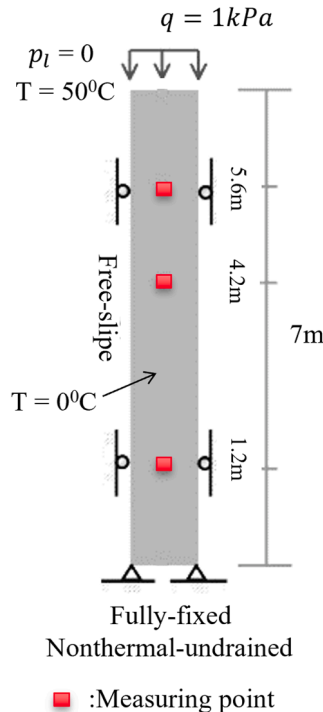


Fig. 17. The geometry and boundary conditions for the one-dimensional THM consolidation problem (After Lei et al., (2021) [19]).

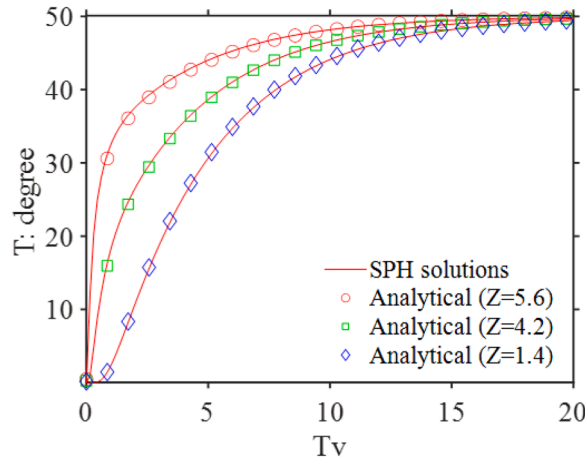


Fig. 18. Temperature evolution at three locations.

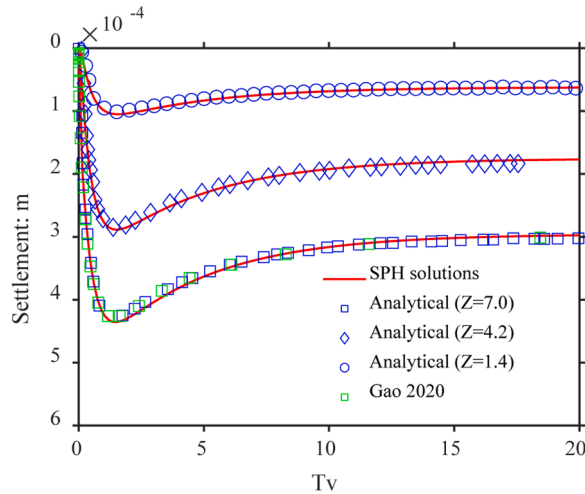


Fig. 19. Displacement profile at three locations.

all three monitoring points. As the soil approaches 50 °C, the expansion becomes less mild, resulting in a flat trend in the curves.

Fig. 20 compares the evolution of excess pore-water pressure in the non-isothermal consolidation problem with solutions by the HM-SPH model (a hydro-mechanical SPH model without thermal effects) in the Terzaghi consolidation problem during the early period ( $T_v < 1.0$ ). The results show that the temperature has a nearly negligible influence on the evolution of excess pore-water pressure in this early consolidation period. Consequently, the THM-SPH model predicts similar results to the isothermal HM-SPH results and the analytical solution. Some minor deviations can be found in the THM-SPH solutions (Fig. 20(a)). This is due to volumetric expansion caused by temperature within the soil column, which deviates the curves from those of the isothermal models. This observation is consistent with the settlement predictions shown in Fig. 17, indicating that the thermal expansion has minor effects on the consolidation process ( $T_v < 1.00$ ).

## 5.5. Thawing-induced slope failure modelling: a hypothesis case study

### 5.5.1. Case description of a hypothesis slope

Thawing-induced slope failure is a typical instability in seasonally frozen and permafrost regions where the soil has been frozen for a long period. The mechanism behind the thawing-induced slope failure involved a complex coupled thermo-hydro-mechanical process that is not fully understood yet. This section employs the proposed coupled THM-SPH framework as the first attempt to address this challenge and showcase its capability in modelling complex multi-physics interactions.

Fig. 21 shows a hypothesis slope with an active frozen soil layer on the permanently frozen rock layer. The term “active” refers to the freezing or thawing that frequently occurs in this layer due to atmospheric temperature, whereas “permanent” stands for the nearly impermeable rock layer that is frozen for a long time and hard to thaw. A groundwater table is assigned at the bottom of the

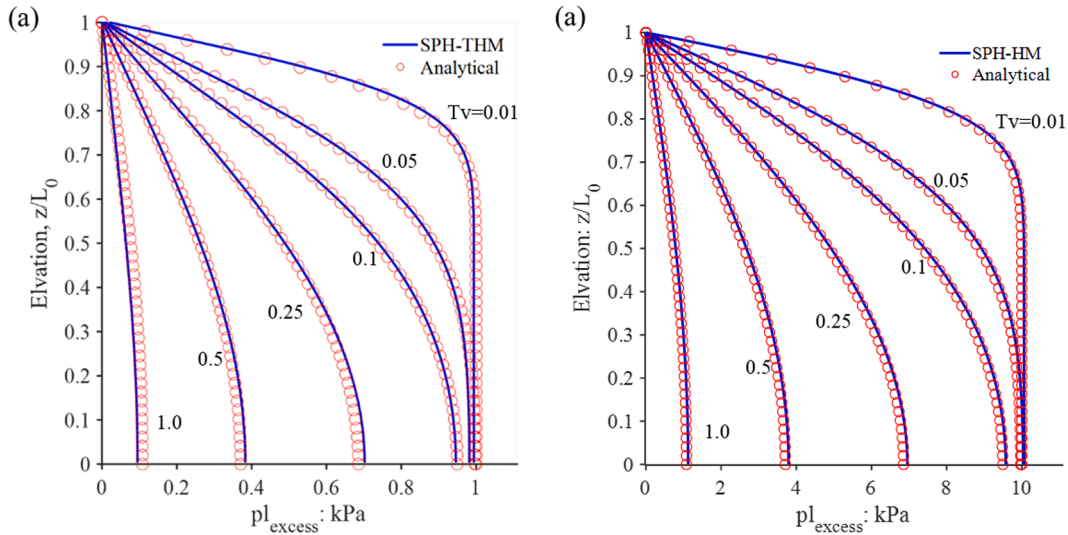


Fig. 20. Excess pore water pressure profile of the whole soil column: (a) THM-SPH approach; (b) HM-SPH approach [16].

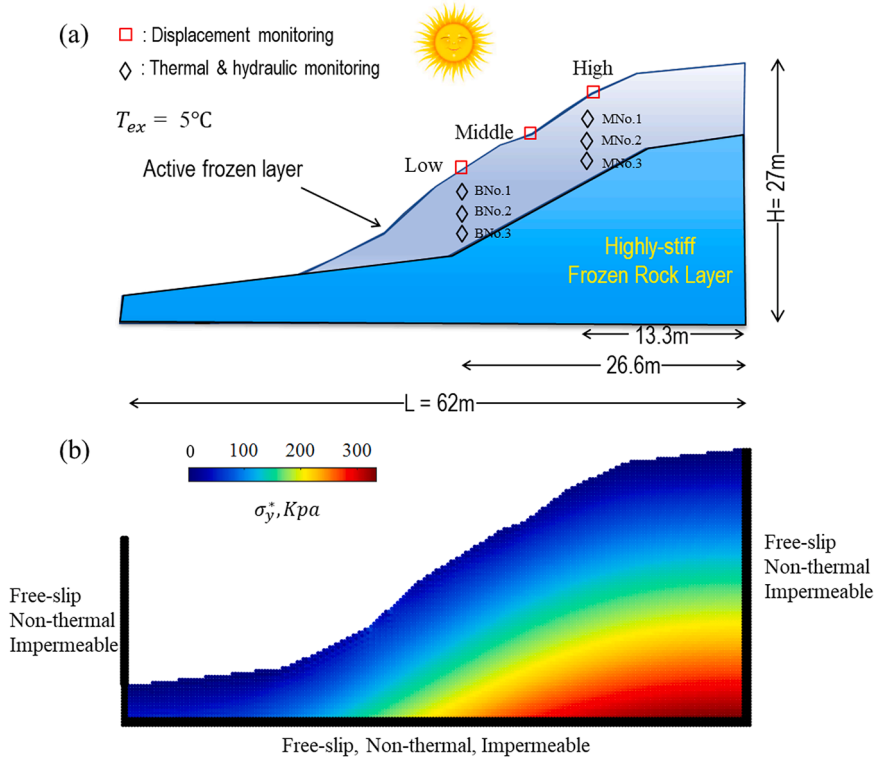


Fig. 21. Geometry and boundary conditions of the slope covered with an active frozen soil layer.

impermanent frozen layer, while a small value of negative pore water pressure of  $p_l = -0.01z$  is assumed to be linearly distributed over the entire slope.

Initially, both soil and rock layers share a permeability of  $2.5 \times 10^{-10}$  m/s. However, for simplicity, the frozen soil is considered impermeable. Upon thawing, the soil becomes saturated, and the permeability will be increased to  $2.5 \times 10^{-8}$  m/s. In the fully thawed region (where the temperature becomes positive), a ponding condition (i.e.,  $p_l=0$ ) is applied to the surface particle to maintain saturation [18]. The material parameters are summarised in Table 5.

For computational efficiency, the frozen rock layer shares the same physical properties as the active frozen soil layer but remains elastic during the simulation. Given the complexity of thermal expansion in frozen soil due to the multi-phase composition, a constant

**Table 5**

Material and model parameters for cryogenic slope failure problems.

	Parameters	Symbol	Value
Mass properties	Soil density ( $\text{kg/m}^3$ )	$\rho_s$	2650
	Ice density ( $\text{kg/m}^3$ )	$\rho_i$	917
	Water density ( $\text{kg/m}^3$ )	$\rho_l$	1000
Mechanical properties	Initial porosity	$n_i$	0.40
	Compression index	$\lambda_0$	0.25
	Swelling index	$\kappa$	0.01
	SI parameter	$\kappa_s$	0.01
	Freezing bring-up stiffness (MPa)	$K_i$	80
	Poisson's ratio	$\nu$	0.3
	Slope of CSL	$M$	0.87
	Bring-up cohesion parameter	$k_t$	0.1
	Segregation threshold (MPa)	$s_0$	7
	LC stiffness coefficient	$r$	0.75
	LC stiffness coefficient ( $\text{kPa}^{-1}$ )	$\beta$	$0.012 \times 10^{-3}$
	Reference pressure (kPa)	$P_r$	1
	Constitutive parameter	$r_c$	2.0
	Constitutive parameter	$n_c$	1.75
	Initial ratio of $p'_0/p^*$	OCR	2.1
	Subloading parameter	$R_0$	15
Thermal properties	Freezing point ( $^{\circ}\text{C}$ )	$T_k$	0.0
	Heat conductivity of soil ( $\text{W/m/K}$ )	$\lambda_s$	4.80
	Heat conductivity of ice ( $\text{W/m/K}$ )	$\lambda_i$	2.22
	Heat conductivity of water ( $\text{W/m/K}$ )	$\lambda_l$	0.6
	Heat capacity of soil ( $\text{J/kg/K}$ )	$c_s$	837
	Heat capacity of ice ( $\text{J/kg/K}$ )	$c_i$	2095
	Heat capacity of water ( $\text{J/kg/K}$ )	$c_l$	4190
	Latent heat of fusion ( $\text{J/kg}$ )	$L_f$	$3.34 \times 10^5$
	Saturated permeability ( $\text{m/s}$ )	$k_l^{\text{sat}}$	$2.5 \times 10^{-8}$
	SFWC parameter ( $\text{Pa}^{-1}$ )	$g_a$	$0.012 \times 10^{-3}$
Hydraulic properties	Maximum ice saturation	$S_{\text{imax}}$	0.985
	SFWC parameter	$g_n$	2.15
	SFWC parameter	$g_c$	0.5348
	Kozeny-Carman coefficient	$C_k$	2
	Water bulk modulus ( $\text{Pa}^{-1}$ )	$n_i/K_i$	$2.57 \times 10^{-7}$

expansion coefficient from the average typical value of soil grain, water and ice [94], i.e.,  $1 \times 10^{-5}/(\text{Pa} \cdot ^{\circ}\text{C})$ , is considered. Additionally, the mechanical behaviour of active frozen soil can vary depending on the constitutive parameters  $r_c$  and  $n_c$  in the original CASM model [63], which will be further examined later in this section.

The above hypothesis frozen slope is modelled by 10,199 particles with an initial spacing distance of 0.3 m. The left and bottom boundaries are isothermal and impermeable, implemented using the seepage boundary approach proposed in the authors' previous work [18]. For mechanical boundaries, the left boundary is treated as a free-slip boundary, while the bottom is modelled as a fully fixed solid boundary, both modelled using the SPH solid boundary approaches proposed by Bui and his co-workers [15]. The slope is initialised with a uniform temperature of  $-5^{\circ}\text{C}$ , and an initial in-situ stress field is established by applying gravitational loading before thawing, as shown in Fig. 21(b) for the mean solid phase stress. Subsequently, the environment temperature is set as  $5^{\circ}\text{C}$  and maintained at the slope surface, enforcing a thermal gradient that drives heat infiltration. To monitor the slope response, three displacement monitoring points (i.e., High, Middle and Low) and six thermal and hydraulic measuring points (MNo.1–3 and BNo.1–3 at depths of 1.2 m, 3 m and 4.2 m) are considered in the slope, as highlighted in Fig. 21(a).

The temperature increase causes the degradation of frozen soil, which will ultimately trigger a cryogenic slope failure. However, this process typically can take a couple of days or even months due to the low thermal conductivity and the significantly large latent heat of fusion in frozen soil. To accelerate the computation, the thermal conductivity and hydraulic permeability are artificially amplified by a factor of 2000, reducing the thawing time scale to hours for efficient demonstration. For numerical integration, the standard explicit scheme is adopted to solve the pore water pressure equation (i.e., Eq. (59)) given the low permeability in this case. In addition, the double-scale time integration scheme proposed in the authors' previous work [16] is also employed to handle the long-term thermal diffusion-triggered thawing failure. The mechanical time step herein is 0.0002 s, and the maximum hydraulic time step is 1.0s, corresponding to a controlling parameter of 5 in this study [16].

### 5.5.2. Thawing-triggered active layer sliding

**5.5.2.1. Qualitative analysis of failure response.** In this SPH simulation of thawing-induced slope failure, we first pay attention to the thermal field and the failure response of the slope, as shown in Fig. 22. The model captures well the warming process where the surface thermal gradient drives the heat infiltration. A melting front, featured by zero temperature, is observed at around  $t = 13.72$  h, as shown in the figure. As the temperature rises, ice close to the ground surface melts, reducing the cryogenic suction and shear strength. This

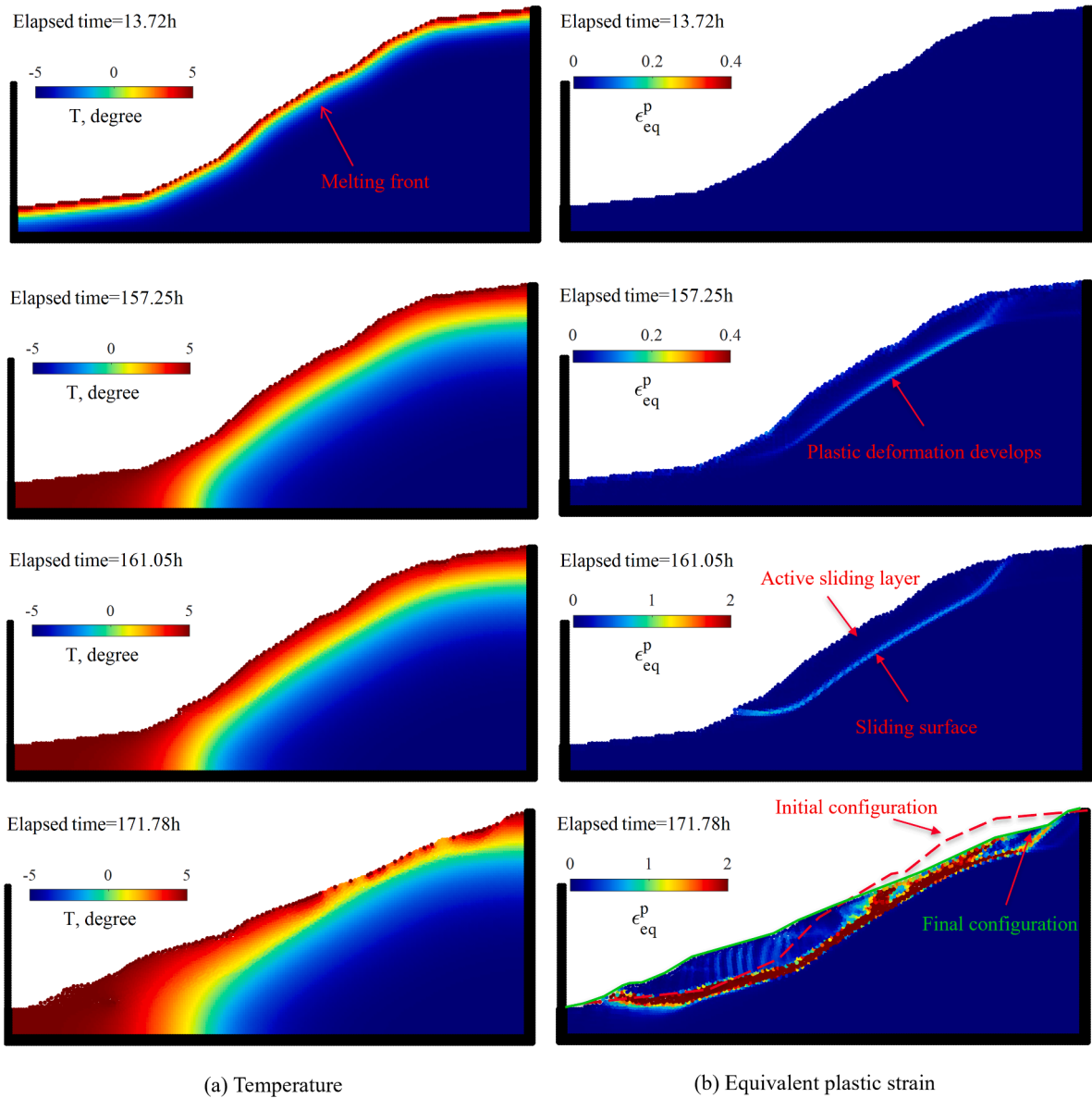


**Fig. 22.** SPH predictions of the evolution of temperature and equivalent plastic strain at different time intervals.

degradation is evidenced by the equivalent plastic strain developed at the crest of the slope in Fig. 22(b). As the heat propagates deeper, the melting front exhibits an expansion in the thickness, indicating an increasing heat diffusion at  $t = 157.25$  h. Additionally, a shear band forms in the active frozen soil layer, driven by water accumulation from melting ice. The increase in pore water weakens the soil, leading to further strength loss and slope destabilisation, as shown in Fig. 22(b).

As the warming continues, ice within the frozen ground melts further, and plastic strain keeps developing. At around  $t = 161.05$  h, a well-defined shear band forms, connecting the middle ground surface to the slope crest. This initiates the rapid downslope movement of the mobilised volume along the frozen-unfrozen interface. Right after the detachment of the mobilised volume flows downward to the trough at the lower elevation, and a secondary slide occurs near the slope crest under gravity due to the loss of lateral support. With the reduced resisting force, more thawed soil progressively flowed downward over the next few hours, as shown in Fig. 22(b). The failure process stops at around 171.78 h, with the initial and final configurations highlighted in Fig. 22(b).

The evolution of pore water pressure and solid-phase stress is presented in Fig. 23. At around  $t = 13.72$  h, a well-defined thawed zone appears near the surface, marked by the positive pore water pressure due to water released from the melting ice. As thawing progresses, more ice melts, and the meltwater migrates downwards under gravity. Due to the low permeability of the frozen layer, water accumulates at the frozen-unfrozen interface, forcing a weakening zone with the pore pressure rising significantly, as seen at  $t = 157.25$  h in Fig. 23(b). Meanwhile, a reduction in constitutive stress in this thawed area can also be observed (Fig. 23(a)). As the

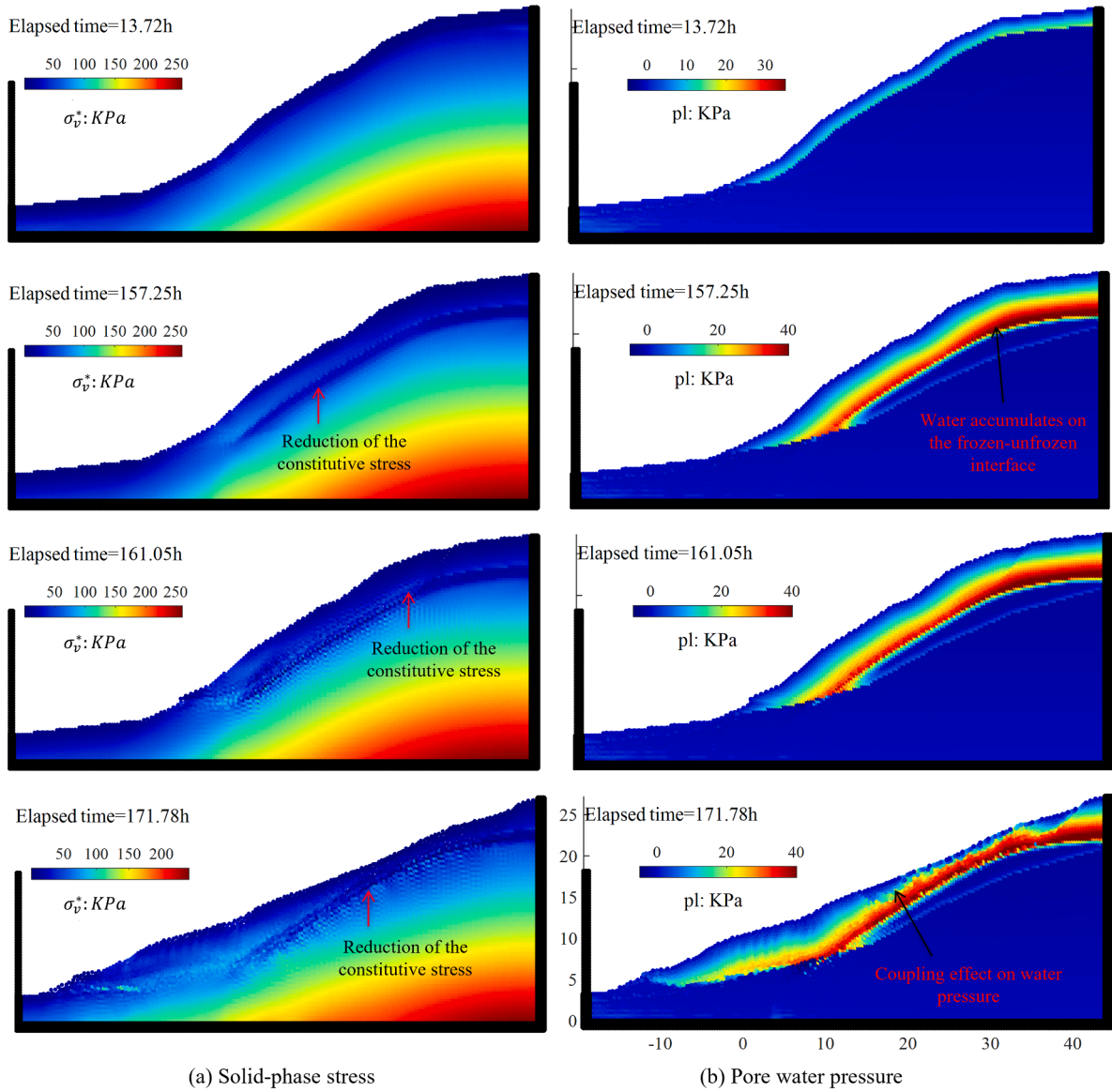


Fig. 23. SPH predictions of the evolution of pore water pressure and mean constitutive stress at different time intervals.

thawing progresses further, more ice melts into water, which further reduces the solid-phase stress and cryogenic suction, decreasing the shear strength. At  $t = 161.05$  h, slope failure occurs as the active layer detaches and slides over the unfrozen-frozen interface. The failure is known as “active layer detachment sliding” in permafrost, which is featured by a cohesive raft of thawed soil sliding over the frozen-thawed interface [1], where the accumulated meltwater further reduces shear strength and encourages sliding.

Overall, the proposed fully coupled THM-SPH framework has demonstrated its capability to capture the entire thawing-induced failure in the active frozen soil layer. To further illustrate its capability, the calculated evolutions of pore water pressure, solid-phase stress, ice content and ice pressure at the outlined measuring points are presented in the subsequent sections.

**5.5.2.2. Quantitative analysis of the thawing process.** Fig. 24 demonstrates the capability of the THM-SPH model in capturing the thawing process by quantitatively analysing the evolutions of temperature, pore ice pressure, ice content and pore water pressure at the measuring locations. The evolution of temperature captured from six monitoring points is presented in Fig. 24(a) and (b), whereas the development of pore-ice pressure and volumetric ice content is given in Figs. 24(c) and 24(d), respectively. Fig. 24(e) and (f) present the pore water pressure changes.

In the middle slope section, monitoring point MNo.1 first responds to the external heat flux around 0.72 h, with an increase in the temperature shown in Fig. 24(a). Correspondingly, the pore ice pressure at this location drops, reaching zero at approximately 12.6 h, indicating complete ice melting. This is further evidenced by a zero temperature, marked by the red dot in Fig. 24(a), and the



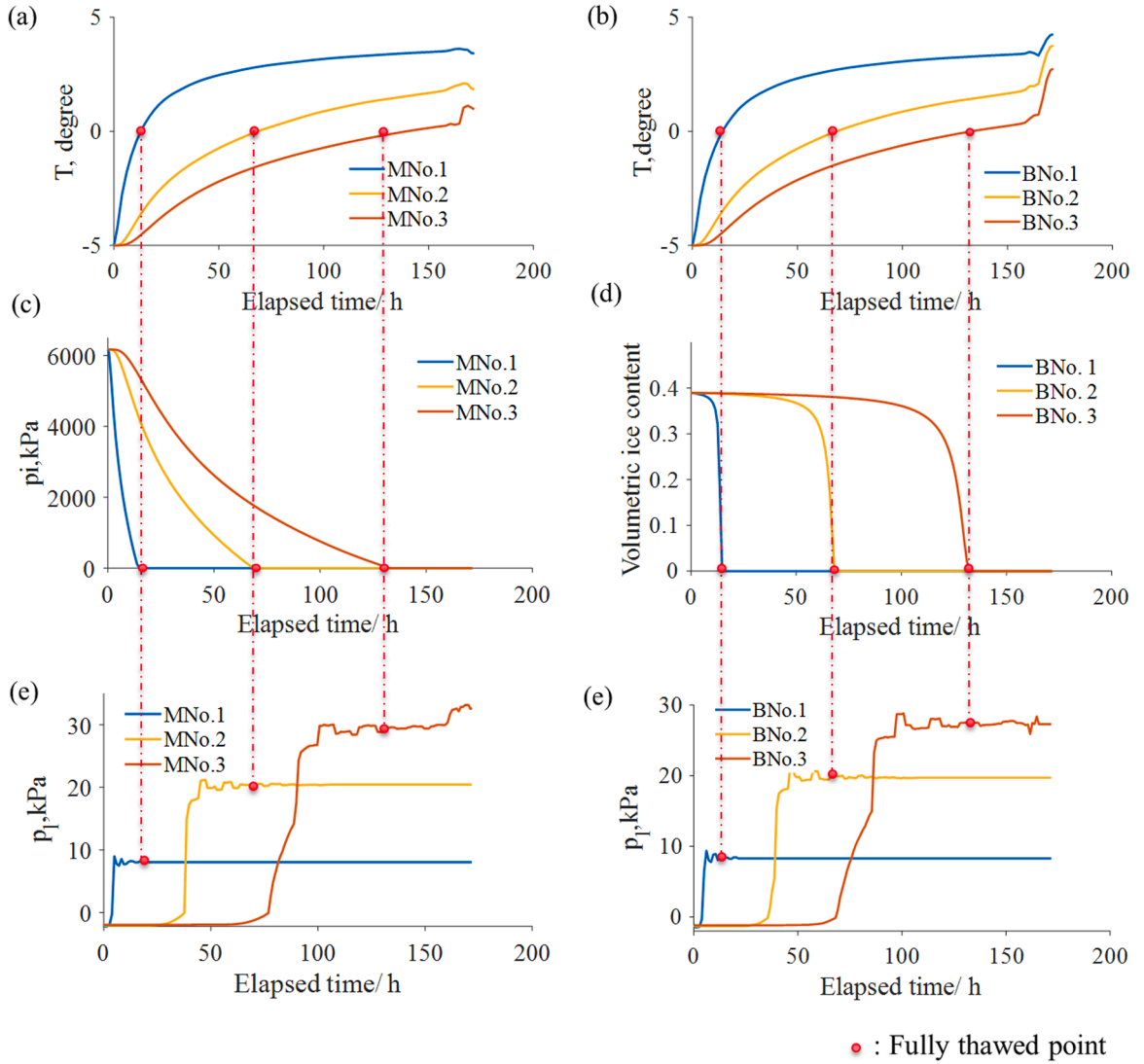


**Fig. 24.** Field quantities analysis of the SPH predictions of thawing-induced slope failure. (a) Temperature at MNo. 1–3; (b) Temperature at BNo. 1–3; (c) pore ice pressure at MNo. 1–3; (d) Ice content at BNo. 1–3; (e) PWP at MNo. 1–3; (f) PWP at BNo. 1–3.

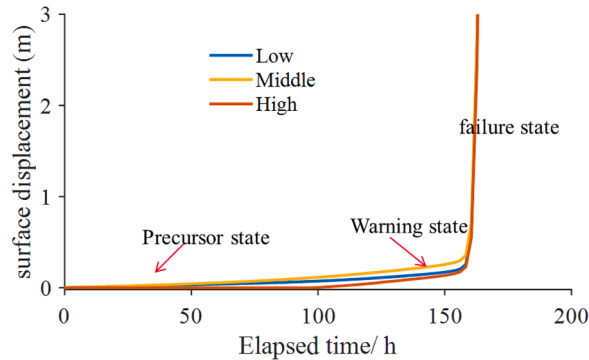


**Fig. 25.** SPH-THM prediction of the evolution of ground displacement.



development of positive pore water pressure (PWP), recorded in Fig. 24(e). Similar trends are observed at points MNo.2 and MNo. 3, which react to the heat flux at around 3.8h and 6.3h, respectively. Interestingly, Fig. 24(a) reveals a decreasing temperature rising rate with depth, suggesting increasing thermal diffusion due to the changes in thermal conductivity. MNo.2 and MNo. 3 reach 0 °C at around 69.0 h and 125.0h, with their pore ice pressure dropping to zero at the same time (Fig. 24(c)). Once ice melting is complete, the pore water pressure of the two locations reaches its equilibrium state, as shown in Fig. 24(e), with point MNo. 3 displaying higher water pressure due to its lower elevation, which collects more meltwater.

Similar trends in the temperature and pore-water pressure are observed in the lower recording points (BNo.1, BNo.2 and BNo.3). The ice melting starts from BNo.1 and fully melts at 12.5 h, coinciding with the temperature surpassing the freezing point (see Fig. 24 (b)). For BNo.2 and BNo.3, ice fully melts at about 68.0 h and 134 h, respectively. Additionally, noticeable fluctuations in the pore water pressure field can be found in Fig. 24(f), which can be attributed to the particle vibration-induced phase changes (i.e., change of bulk modulus and reduction of shear strength). These changes affect the solid-phase stress, resulting in particle re-distribution and minor volumetric strain. Notably, such an effect can only be captured using a fully coupled THM model.

One crucial aspect in a slope failure forecast and prevention system design is to monitor the ground surface displacement, requiring a computational approach capable of capturing the deformation throughout the entire thawing process. Fig. 25 demonstrates that the proposed framework effectively tracks the ground displacement. During the first hour, the “High” monitoring point initially captures a displacement of around 0.06 m due to phase change. This is considered the precursor state, where minor ground displacements are

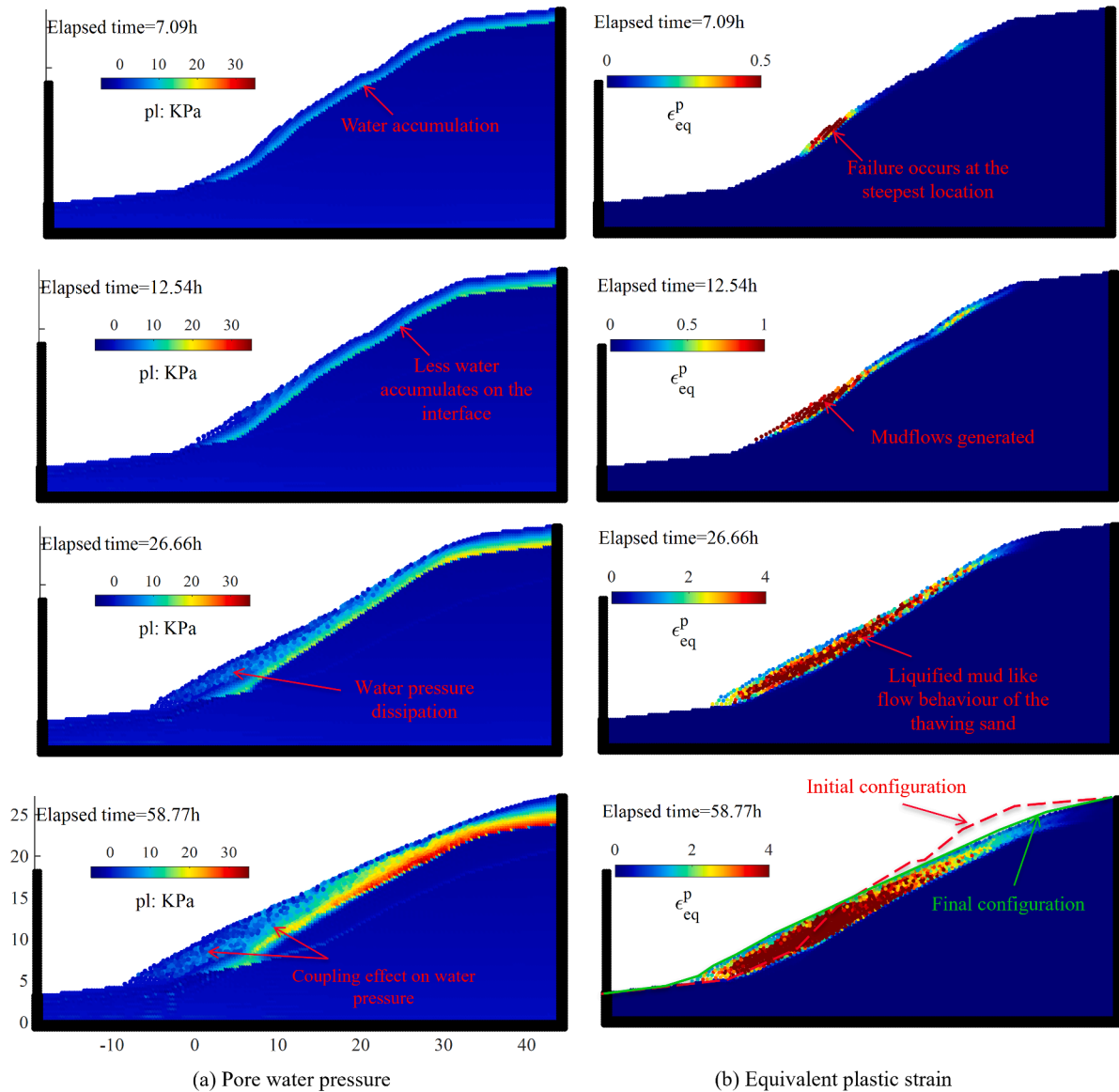


Fig. 26. SPH predictions of the evolution of temperature and equivalent plastic strain at different time intervals in the slope of sandy material.

noticed while the slope remains stable. However, after around 100 h, displacement at three monitoring points starts to accelerate, indicating a shift into the warning state, where the slope failure is about to occur. This acceleration is primarily driven by the increased water content, as analysed above, reducing both solid-phase stress and shear strength. Eventually, at around 171.0 h, the slope collapses, as evidenced by the non-converged displacement curve. Tracking deformation information over time is critical for failure monitoring, disaster prevention, and early warning systems, and the results highlight the potential of the proposed coupled THM-SPH framework in the application of developing disaster prevention systems for thawing-induced landslides.

### 5.5.3. Thawing-induced retrogressive slope failure

The previous section demonstrated the capability of the proposed THM-SPH framework in simulating a deep active layer detachment, a failure mode where the active layer of cohesive soil slides over a thawed boundary in permafrost [1]. This section extends the analysis to thawing collapse in frozen sandy soils, a different failure mode influenced by soil type.

As noted by Yu (1998) [59], the CASM model is a unified model capable of describing both clay and sand, which is achieved by adjusting the constitutive parameters ( $n_c$ ,  $r_c$ ) that control the shape of the yield surface [59]. The previous section focused on frozen clay behaviour ( $n_c=1.75$ ,  $r_c=2.0$ ), while in this section, we will explore the failure behaviour of frozen sand by adjusting  $n_c=1.75$  and  $r_c=108$ , as recommended by Yu (1998) [59]. The same simulation setup as conducted in Section 5.5.2 is repeated with all other parameters kept the same. Additionally, to reflect the ice-rich nature of sand, the porosity of the materials is increased to 0.5.

Fig. 26 illustrates the thawing-induced slope failure process in terms of pore-water pressure evolution and accumulated equivalent plastic strain. Unlike frozen clays, a different failure mechanism is observed. For example, after around 7.09 h, plastic strain is observed at the steepest location, and the plastic strain becomes significant at 12.54 h, indicating the initiation of thaw failure. Progressive ice melting leads to shallow sliding, exhibiting mudflow-like sliding behaviour (see Fig. 26(b)). This is attributed to the nearly complete loss of cementing bonds between sand particles when ice melts.

Compared to clays, thawed sand accumulates less water in the thawed zone due to the large porosity that facilitates the melted water to seep out of the slope. Nevertheless, shear strength reduction due to ice melting promotes a backward progressive failure from the lower elevation to the slope crest. By  $t = 26.66$  h, the unfrozen soil flows downwards in a liquified mud flow manner, highlighting a retrogressive thaw flow. This failure mechanism is commonly found in ice-rich frozen soil, and it differs greatly from the active layer sliding, where the cohesive force in clays stabilises the slope, and the failure does not occur until a certain depth of thawing [1]. The flowing sand accumulates at the slope toe, providing lateral resistance that stops further failure of the slope at around 58.77 h (Fig. 26(b)). Specifically, the observed retrogressive thawing sliding behaviour highlights the ability of the framework to capture different thawing-induced failure mechanisms in different frozen soil materials.

The proposed computational THM-SPH framework is demonstrated in predicting the thawing-induced collapse of slopes of different frozen soil materials. To the authors' best knowledge, this is the first successful SPH modelling approach for simulating thawing-induced slope collapse while incorporating the coupled THM processes and materials failure behaviour. While lab or field data may be required for further validation, the results suggest that the proposed THM-SPH framework provides a mesh-free approach for modelling large-scale thawing-induced large deformation slope failures. The framework has also demonstrated its capability in capturing key multiphase, multi-physics interactions in coupled THM systems, offering an efficient computational tool for investigating complex geotechnical processes.

## 6. Conclusion

This paper presents the first fully coupled THM-SPH computational framework to address one of the most challenging geotechnical problems, i.e., thawing-triggered slope failure, by solving the fully coupled heat-flow-soil interactions in frozen soils. Compared to the existing coupled flow-deformation SPH framework for unsaturated/saturated soils, an advancement has been made by coupling the extra heat/temperature in the framework, thus enabling the fully coupled thermo-hydro-mechanical (THM) process to be assessed. More importantly, an advanced constitutive model for frozen soil (CASM-F) was introduced into the proposed THM-SPH framework to enable the description of the transition response and large deformation behaviour of frozen soils due to thawing action for the first time. The proposed computational framework was verified against several well-known analytical solutions and literature results before being applied to simulate a hypothesis thawing-triggered slope failure involving multiphase multi-physics processes. It is demonstrated throughout this paper that the proposed THM-SPH framework can effectively capture the influence of heat transfer on the ice-melting and water accumulation processes and the subsequent collapse of frozen soil slopes. To the best of the authors' knowledge, this is the first fully coupled SPH computational framework capable of handling such a complex multi-physics process. On the basis of this success, future studies include extending the framework to full 3D conditions, together with comparisons with field and laboratory data on unsaturated-unfrozen soils to further validate and enhance the predictive capability of the proposed framework and models.

### CRediT authorship contribution statement

**Yanjian Lian:** Writing – original draft, Visualization, Validation, Software, Methodology, Investigation, Formal analysis, Data curation. **Ha H. Bui:** Writing – review & editing, Supervision, Software, Resources, Project administration, Methodology, Investigation, Funding acquisition, Formal analysis, Conceptualization. **Giang D. Nguyen:** Writing – review & editing, Supervision, Methodology, Investigation.

## Declaration of competing interest

The authors declare that they have no known competing financial interests or personal relationships that could have appeared to influence the work reported in this paper.

## Acknowledgement

The authors gratefully acknowledge support from the Australian Research Council via DP190102779 (Bui & Nguyen), FT200100884 (Bui), DP240102765 (Bui & Nguyen) and LP220200792 (Bui & Nguyen). Part of this research was undertaken with the assistance of resources and services from the National Computational Infrastructure (NCI), supported by the Australian Government. The support of the China Scholarship Council (CSC, No. 201906050025) is also gratefully acknowledged.

## Data availability

Data will be made available on request.

## References

- [1] J. van Huissteden, Thawing Permafrost, Springer International Publishing, Cham, 2020, <https://doi.org/10.1007/978-3-030-31379-1>.
- [2] B.W. Abbott, J.B. Jones, Permafrost collapse alters soil carbon stocks, respiration, CH<sub>4</sub>, and N<sub>2</sub>O in upland tundra, *Glob. Change Biol.* 21 (2015) 4570–4587, <https://doi.org/10.1111/gcb.13069>.
- [3] S.V. Kokelj, D. Lacelle, T.C. Lantz, J. Tunnicliffe, L. Malone, I.D. Clark, K.S. Chin, Thawing of massive ground ice in mega slumps drives increases in stream sediment and solute flux across a range of watershed scales, *Int. J. Geogr. Inf. Sci.* 118 (2013) 681–692, <https://doi.org/10.1002/jgrf.20063>.
- [4] S. Nishimura, A. Gens, S. Olivella, R.J. Jardine, Thm-coupled finite element analysis of frozen soil: formulation and application, *Geotechnique* 59 (2009) 159–171, <https://doi.org/10.1680/geot.2009.59.3.159>.
- [5] O.B. Andersland, B. Ladanyi, Mechanical properties of frozen soils. An Introduction to Frozen Ground Engineering, Springer US, Boston, MA, 1994, pp. 121–150, [https://doi.org/10.1007/978-1-4757-2290-1\\_5](https://doi.org/10.1007/978-1-4757-2290-1_5).
- [6] C. Lyu, S. Nishimura, S.A.G. Amiri, F. Zhu, G.R. Eiksund, G. Grimstad, Pore-water pressure development in a frozen saline clay under isotropic loading and undrained shearing, *Acta Geotech.* 16 (2021) 3831–3847, <https://doi.org/10.1007/s11440-021-01338-y>.
- [7] X. Xu, Y. Lai, Y. Dong, J. Qi, Laboratory investigation on strength and deformation characteristics of ice-saturated frozen sandy soil, *Cold Reg. Sci. Technol.* 69 (2011) 98–104, <https://doi.org/10.1016/j.coldregions.2011.07.005>.
- [8] Y. Lai, L. Jin, X. Chang, Yield criterion and elasto-plastic damage constitutive model for frozen sandy soil, *Int. J. Plast.* 25 (2009) 1177–1205, <https://doi.org/10.1016/j.ijplas.2008.06.010>.
- [9] S. Nishimura, A model for freeze-thaw-induced plastic volume changes in saturated clays, *Soils Found.* 61 (2021) 1054–1070, <https://doi.org/10.1016/j.sandf.2021.05.008>.
- [10] S.A. Ghoreishian Amiri, G. Grimstad, M. Kadivar, S. Nordal, Constitutive model for rate-independent behavior of saturated frozen soils, *Can. Geotech. J.* 53 (2016) 1646–1657, <https://doi.org/10.1139/cgj-2015-0467>.
- [11] Y. Zhang, Thermal-hydro-mechanical model for freezing and thawing of soils, (2014) 201.
- [12] S.H. Na, W.C. Sun, Computational thermo-hydro-mechanics for multiphase freezing and thawing porous media in the finite deformation range, *Comput. Methods Appl. Mech. Eng.* 318 (2017) 667–700, <https://doi.org/10.1016/j.cma.2017.01.028>.
- [13] H.R. Thomas, P. Cleall, Y.C. Li, C. Harris, M. Kern-Luetsch, Modelling of cryogenic processes in permafrost and seasonally frozen soils, *Geotechnique* 59 (2009) 173–184, <https://doi.org/10.1680/geot.2009.59.3.173>.
- [14] J. Rutqvist, L. Zheng, F. Chen, H.H. Liu, J. Birkholzer, Modeling of coupled thermo-hydro-mechanical processes with links to geochemistry associated with bentonite-backfilled repository tunnels in clay formations, *Rock Mech. Rock Eng.* 47 (2014) 167–186, <https://doi.org/10.1007/s00603-013-0375-x>.
- [15] H.H. Bui, G.D. Nguyen, Smoothed particle hydrodynamics (SPH) and its applications in geomechanics: from solid fracture to granular behaviour and multiphase flows in porous media, *Comput. Geotech.* 138 (2021) 104315, <https://doi.org/10.1016/j.compgeo.2021.104315>.
- [16] Y. Lian, H.H. Bui, G.D. Nguyen, S. Zhao, A. Haque, A computationally efficient SPH framework for unsaturated soils and its application to predicting the entire rainfall-induced slope failure process, *Geotechnique* (2022), <https://doi.org/10.1680/jgeot.21.00349>.
- [17] Y. Lian, H.H.H. Bui, G.D.G.D. Nguyen, A. Haque, An effective and stabilised (u – p) SPH framework for large deformation and failure analysis of saturated porous media, *Comput. Methods Appl. Mech. Eng.* 408 (2023) 115967, <https://doi.org/10.1016/j.cma.2023.115967>.
- [18] Y. Lian, H.H.H. Bui, G.D.G.D. Nguyen, H.T.H.T. Tran, A. Haque, A general SPH framework for transient seepage flows through unsaturated porous media considering anisotropic features of diffusion, *Comput. Methods Appl. Mech. Eng.* 387 (2021) 114169, <https://doi.org/10.1016/j.cma.2021.114169>.
- [19] X. Lei, S. He, A. Abed, X. Chen, Z. Yang, Y. Wu, A generalized interpolation material point method for modelling coupled thermo-hydro-mechanical problems, *Comput. Methods Appl. Mech. Eng.* 386 (2021) 114080, <https://doi.org/10.1016/j.cma.2021.114080>.
- [20] J. Yu, J. Zhao, S. Zhao, W. Liang, Thermo-hydro-mechanical coupled material point method for modeling freezing and thawing of porous media, *Numer. Anal. Methods Geomech.* 48 (2024) 3308–3349, <https://doi.org/10.1002/nag.3794>.
- [21] Z.Q. Zhan, C. Zhou, C.Q. Liu, J.T. Du, MPM formulations for the coupled thermo-hydro-mechanical behaviour of saturated and unsaturated soils, *Comput. Geotech.* 170 (2024) 106313, <https://doi.org/10.1016/j.compgeo.2024.106313>.
- [22] L.B. Lucy, A numerical approach to the testing of the fission hypothesis, 82 (1977) 1013–1024.
- [23] A.R. Gingold, J.J. Monaghan, Smoothed particle hydrodynamics: theory and application to non-spherical stars, 181 (1977) 375–389.
- [24] H.H. Bui, R. Fukagawa, K. Sako, S. Ohno, Lagrangian meshfree particles method (SPH) for large deformation and failure flows of geomaterial using elasto-plastic soil constitutive model, *Int. J. Numer. Anal. Methods Geomech.* 32 (2008) 1537–1570, <https://doi.org/10.1002/nag>.
- [25] H.H. Bui, Lagrangian Mesh-free Particle Method (SPH) For Large Deformation and Post-failure of Geomaterial using Elasto-plastic Constitutive Models, Ritsumeikan University, 2006. [http://r-cube.ritsumei.ac.jp/repo/repository/rcube/9152/k.466\\_e.htm](http://r-cube.ritsumei.ac.jp/repo/repository/rcube/9152/k.466_e.htm).
- [26] A.H.F. Neto, R.I. Borja, A.H. Fávoro Neto, R.I. Borja, Continuum hydrodynamics of dry granular flows employing multiplicative elastoplasticity, *Acta Geotech.* 3 (2018) 1027–1040, <https://doi.org/10.1007/s11440-018-0700-3>.
- [27] C.M. Chalk, M. Pastor, J. Peakall, D.J. Borman, P.A. Sleight, W. Murphy, R. Fuentes, C. Methods, A. Mech, C.M. Chalk, M. Pastor, J. Peakall, D.J. Borman, P. A. Sleight, W. Murphy, R. Fuentes, Stress-particle smoothed particle hydrodynamics : an application to the failure and post-failure behaviour of slopes, *Comput. Methods Appl. Mech. Eng.* 366 (2020) 113034, <https://doi.org/10.1016/j.cma.2020.113034>.
- [28] C.T. Nguyen, C.T. Nguyen, H.H. Bui, G.D. Nguyen, R. Fukagawa, A new SPH-based approach to simulation of granular flows using viscous damping and stress regularisation, *Landslides* 14 (2017) 69–81, <https://doi.org/10.1007/s10346-016-0681-y>.
- [29] E. Yang, H.H. Bui, H. De Sterck, G.D. Nguyen, A. Bouazza, A scalable parallel computing SPH framework for predictions of geophysical granular flows, *Comput. Geotech.* 121 (2020) 103474, <https://doi.org/10.1016/j.compgeo.2020.103474>.

- [30] H.H. Bui, R. Fukagawa, K. Sako, J.C. Wells, Slope stability analysis and discontinuous slope failure simulation by elasto-plastic smoothed particle hydrodynamics (SPH), *Geotechnique* 61 (2011) 565–574, <https://doi.org/10.1680/geot.9.P.046>.
- [31] X. He, D. Liang, M.D. Bolton, Run-out of cut-slope landslides: mesh-free simulations, *Geotechnique* 68 (2018) 50–63, <https://doi.org/10.1680/jgeot.16.P.221>.
- [32] H.H. Bui, R. Fukagawa, An improved SPH method for saturated soils and its application to investigate the mechanisms of embankment failure: case of hydrostatic pore-water pressure, *Int. J. Numer. Anal. Methods Geomech.* 37 (2013) 31–50, <https://doi.org/10.1002/nag.1084>.
- [33] M. Pastor, T. Blanc, B. Haddad, S. Petrone, M. Sanchez Morles, V. Drempetic, D. Issler, G.B. Crosta, L. Cascini, G. Sorbino, S. Cuomo, Application of a SPH depth-integrated model to landslide run-out analysis, *Landslides* 11 (2014) 793–812, <https://doi.org/10.1007/s10346-014-0484-y>.
- [34] T. Blanc, M. Pastor, A stabilized runge-kutta, taylor smoothed particle hydrodynamics algorithm for large deformation problems in dynamics, *Int. J. Numer. Methods Eng.* 91 (2012) 1427–1458, <https://doi.org/10.1002/nme.4324>.
- [35] C. Cai, W. Ma, Z. Zhou, Y. Mu, S. Zhao, D. Chen, M. Liao, Laboratory investigation on strengthening behavior of frozen China standard sand, *Acta Geotech.* 14 (2019) 179–192, <https://doi.org/10.1007/s11440-018-0648-3>.
- [36] E. Yang, H.H. Bui, G.D. Nguyen, C.E. Choi, C.W.W. Ng, H. De Sterck, A. Bouazza, Numerical investigation of the mechanism of granular flow impact on rigid control structures, *Acta Geotech.* (2021), <https://doi.org/10.1007/s11440-021-01162-4>.
- [37] B. Sheikh, T. Qiu, A. Ahmadipour, Comparison of SPH boundary approaches in simulating frictional soil–structure interaction, *Acta Geotech.* (2020) 1–20, <https://doi.org/10.1007/s11440-020-01063-y>.
- [38] H.H. Bui, J.K. Kodikara, A. Bouazza, A. Haque, P.G. Ranjith, A novel computational approach for large deformation and post-failure analyses of segmental retaining wall systems, *Int. J. Numer. Anal. Methods Geomech.* 38 (2014) 1321–1340, <https://doi.org/10.1002/nag.2253>.
- [39] H.T. Tran, Y. Wang, G.D. Nguyen, J. Kodikara, M. Sanchez, H.H. Bui, Modelling 3D desiccation cracking in clayey soils using a size-dependent SPH computational approach, *Comput. Geotech.* 116 (2019) 103209, <https://doi.org/10.1016/j.compgeo.2019.103209>.
- [40] H.T. Tran, N.H.T. Nguyen, G.D. Nguyen, H.H. Bui, Meshfree SPH modelling of shrinkage induced cracking in clayey soils, *Lect. Notes Civ. Eng.* 54 (2020) 889–894, [https://doi.org/10.1007/978-981-15-0802-8\\_142](https://doi.org/10.1007/978-981-15-0802-8_142).
- [41] Y. Wang, H.T. Tran, G.D. Nguyen, P.G. Ranjith, H.H. Bui, Simulation of mixed-mode fracture using SPH particles with an embedded fracture process zone, *Int. J. Numer. Anal. Methods Geomech.* 44 (2020) 1417–1445, <https://doi.org/10.1002/nag.3069>.
- [42] Y. Wang, H.H. Bui, G.D. Nguyen, P.G. Ranjith, A new SPH-based continuum framework with an embedded fracture process zone for modelling rock fracture, *Int. J. Solids Struct.* 159 (2019) 40–57, <https://doi.org/10.1016/j.ijsolstr.2018.09.019>.
- [43] S. Gharehdash, L. Shen, Y. Gan, Numerical study on mechanical and hydraulic behaviour of blast-induced fractured rock, *Eng. Comput.* 36 (2020) 915–929, <https://doi.org/10.1007/s00366-019-00740-1>.
- [44] Z. Li, V.T. Le, G.D. Nguyen, H.H. Bui, Rate-dependent constitutive modelling of dynamic fracture in quasi-brittle materials, *Int. J. Rock Mech. Min. Sci.* 191 (2025) 106122, <https://doi.org/10.1016/j.ijrmms.2025.106122>.
- [45] V.T. Le, Tien.V. Nguyen, N.T. Nguyen, G.D. Nguyen, M. Karakus, H.H. Bui, A simple 3D damage-plasticity model with energy-based regularisation in SPH for modelling fractured quasi-brittle rocks, *Rock Mech. Rock Eng.* (2025), <https://doi.org/10.1007/s00603-025-04638-x>.
- [46] H.H. Bui, K. Sako, R. Fukagawa, Numerical simulation of soil-water interaction using smoothed particle hydrodynamics (SPH) method, *J. Terramech.* 44 (2007) 339–346, <https://doi.org/10.1016/j.jterra.2007.10.003>.
- [47] H.H. Bui, G.D. Nguyen, A coupled fluid-solid SPH approach to modelling flow through deformable porous media, *Int. J. Solids Struct.* 125 (2017) 244–264, <https://doi.org/10.1016/j.ijsolstr.2017.06.022>.
- [48] K. Maeda, H. Sakai, M. Sakai, Development of seepage failure analysis method of ground with smoothed particle hydrodynamics, *Struct. Eng. /Earthq. Eng.* 23 (2006) 307s–319s, <https://doi.org/10.2208/JSCSEEE.23.307S>.
- [49] H.H. Bui, R. Fukagawa, A first attempt to solve soil water coupled problems by SPH, *Jpn. Terramech* 29 (2008) 30–38.
- [50] M. Pastor, B. Haddad, G. Sorbino, S. Cuomo, V. Drempetic, A depth-integrated, coupled SPH model for flow-like landslides and related phenomena, *Int. J. Numer. Anal. Methods Geomech.* 33 (2009) 143–172, <https://doi.org/10.1002/NAG.705>.
- [51] D.S. Morikawa, M. Asai, Soil-water strong coupled ISPH based on u–w–p formulation for large deformation problems, *Comput. Geotech.* 142 (2022) 104570, <https://doi.org/10.1016/j.compgeo.2021.104570>.
- [52] G. Ma, H.H. Bui, Y. Lian, K.M. Tran, G.D. Nguyen, A five-phase approach, SPH framework and applications for predictions of seepage-induced internal erosion and failure in unsaturated/saturated porous media, *Comput. Methods Appl. Mech. Eng.* 401 (2022), <https://doi.org/10.1016/j.cma.2022.115614>.
- [53] T.N. Hoang, T.T. Nguyen, T.V. Nguyen, G.D. Nguyen, H.H. Bui, SPH simulation of earthquake-induced liquefaction and large deformation behaviour of granular materials using SANISAND constitutive model, *Comput. Geotech.* 174 (2024) 106617, <https://doi.org/10.1016/j.compgeo.2024.106617>.
- [54] T.N. Hoang, H.H. Bui, T.T. Nguyen, T.V. Nguyen, G.D. Nguyen, Development of free-field and compliant base SPH boundary conditions for large deformation seismic response analysis of geomechanics problems, *Comput. Methods Appl. Mech. Eng.* 432 (2024) 117370, <https://doi.org/10.1016/j.cma.2024.117370>.
- [55] G. Ma, H.H. Bui, Y. Lian, T.V. Nguyen, G.D. Nguyen, Prediction of backward erosion, pipe formation and induced failure using a multi-physics SPH computational framework, *Int. J. Numer. Anal. Methods Geomech.* (2024) 1–20, <https://doi.org/10.1002/nag.3847>.
- [56] R. Feng, G. Fourtakas, B.D. Rogers, D. Lombardi, Two-phase fully-coupled smoothed particle hydrodynamics (SPH) model for unsaturated soils and its application to rainfall-induced slope collapse, *Comput. Geotech.* 151 (2022) 104964, <https://doi.org/10.1016/j.compgeo.2022.104964>.
- [57] D.T. Nguyen, H.H. Bui, Y. Lian, T.T. Nguyen, G.D. Nguyen, A. Bouazza, A CASM-X constitutive model for unsaturated soils and its application to model wetting-induced slope collapse, *Comput. Geotech.* 186 (2025) 107353, <https://doi.org/10.1016/j.compgeo.2025.107353>.
- [58] Y.W. Bekele, H. Kyokawa, A.M. Kvarving, T. Kvamsdal, S. Nordal, Isogeometric analysis of THM coupled processes in ground freezing, *Comput. Geotech.* 88 (2017) 129–145, <https://doi.org/10.1016/j.compgeo.2017.02.020>.
- [59] Y. Lian, H.H. Bui, G.D. Nguyen, S. Zhao, A. Haque, A computationally efficient SPH framework for unsaturated soils and its application to predicting the entire rainfall-induced slope failure process, *Geotechnique* 74 (2024) 787–805, <https://doi.org/10.1680/jgeot.21.00349>.
- [60] M.Th. van Genuchten, M.Th. van Genuchten, M.Th. van Genuchten, A closed-form equation for predicting the hydraulic conductivity of unsaturated soils, *Soil Sci. Soc. Am. J.* 44 (1980) 892–898, <https://doi.org/10.2136/sssaj1980.03615995004400050002x>.
- [61] S. Nishimura, J. Wang, A simple framework for describing strength of saturated frozen soils as multi-phase coupled system, *Geotechnique* 69 (2019) 659–671, <https://doi.org/10.1680/jgeot.17.P.104>.
- [62] K. Sun, A. Zhou, A multisurface elastoplastic model for frozen soil, *Acta Geotech.* 16 (2021) 3401–3424, <https://doi.org/10.1007/s11440-021-01391-7>.
- [63] H.S. Yu, CASM: a unified state parameter model for clay and sand, *Int. J. Numer. Anal. Methods Geomech.* 22 (1998) 621–653, [https://doi.org/10.1002/\(SICI\)1096-9853\(199808\)22:8<621::AID-NAG937>3.0.CO;2-8](https://doi.org/10.1002/(SICI)1096-9853(199808)22:8<621::AID-NAG937>3.0.CO;2-8).
- [64] E.E. Alonso, A constitutive model for partially saturated soils, *Geotechnique* 41 (1991) 273–275, <https://doi.org/10.1680/geot.1991.41.2.273>.
- [65] N. Khalili, E. Romero, F.A.M. Marinoni, State of the art report. Advances in unsaturated soil mechanics: constitutive modelling, experimental investigation, and field I, in: *Proceedings of the 20th ICSMGE-State of the Art and Invited Lectures – Rahman and Jaksa (Eds) © 2022 Australian Geomechanics*, 2022, pp. 297–348.
- [66] D. Sheng, Review of fundamental principles in modelling unsaturated soil behaviour, *Comput. Geotech.* 38 (2011) 757–776, <https://doi.org/10.1016/j.compgeo.2011.05.002>.
- [67] A. Gens, Soil-environment interactions in geotechnical engineering, *Geotechnique* 60 (2010) 3–74, <https://doi.org/10.1680/geot.9.P.109>.
- [68] D.G. Phan, G.D. Nguyen, H.H. Bui, T. Bennett, Constitutive modelling of partially saturated soils: hydro-mechanical coupling in a generic thermodynamics-based formulation, *Int. J. Plast.* 136 (2021) 102821, <https://doi.org/10.1016/j.iplas.2020.102821>.
- [69] W. Mun, J.S. McCartney, Constitutive model for drained compression of unsaturated clay to high stresses, *J. Geotech. Geoenviron. Eng.* 143 (2017) 1–11, [https://doi.org/10.1061/\(asce\)gt.1943-5606.0001662](https://doi.org/10.1061/(asce)gt.1943-5606.0001662).
- [70] S.J. Wheeler, D. Gallipoli, M. Karstunen, Comments on use of the Barcelona Basic Model for unsaturated soils, *Int. J. Numer. Anal. Methods Geomech.* 26 (2002) 1561–1571, <https://doi.org/10.1002/nag.259>.

- [71] A.N. Zhou, D. Sheng, S.W. Sloan, A. Gens, Interpretation of unsaturated soil behaviour in the stress - saturation space, I: volume change and water retention behaviour, *Comput. Geotech.* 43 (2012) 178–187, <https://doi.org/10.1016/j.compgeo.2012.04.010>.
- [72] P.W. Rowe, The stress-dilatancy relation for static equilibrium of an assembly of particles in contact, *Proc. R. Soc. Lond., A. Math. Phys. Sci.* 269 (1962) 500–527, <https://doi.org/10.1098/rspa.1962.0193>.
- [73] S.J. Wheeler, R.S. Sharma, M.S.R. Buisson, Coupling of hydraulic hysteresis and stress-strain behaviour in unsaturated soils, *Geotechnique* 53 (2003) 41–54, <https://doi.org/10.1680/geot.2003.53.1.41>.
- [74] K. Hashiguchi, Subloading surface model in unconventional plasticity, *Int. J. Solids Struct.* 25 (1989) 917–945, [https://doi.org/10.1016/0020-7683\(89\)90038-3](https://doi.org/10.1016/0020-7683(89)90038-3).
- [75] K. Hashiguchi, Y. Yamakawa, T. Anjiki, M. Ueno, Comprehensive review of subloading surface model: governing law of irreversible mechanical phenomena of solids, *Arch. Comput. Methods Eng.* 31 (2024) 1579–1609, <https://doi.org/10.1007/s11831-023-10022-1>.
- [76] G. Xu, W. Wu, J. Qi, An extended hypoplastic constitutive model for frozen sand, *Soils Found.* 56 (2016) 704–711, <https://doi.org/10.1016/j.sandf.2016.07.010>.
- [77] P.W. Cleary, J.J. Monaghan, Conduction modelling using smoothed particle hydrodynamics, *J. Comput. Phys.* 148 (1999) 227–264, <https://doi.org/10.1006/jcph.1998.6118>.
- [78] P. Español, M. Revenga, Smoothed dissipative particle dynamics, *Phys. Rev. Stat. Phys. Plasmas Fluids Relat. Interdiscip. Top.* 67 (2003) 12, <https://doi.org/10.1103/PhysRevE.67.026705>.
- [79] S. Biriukov, D.J. Price, Stable anisotropic heat conduction in smoothed particle hydrodynamics, *Mon. Not. R. Astron. Soc.* 483 (2019) 4901–4909, <https://doi.org/10.1093/mnras/sty3413>.
- [80] T. Tran-Duc, E. Bertevas, N. Phan-Thien, B.C. Khoo, Simulation of anisotropic diffusion processes in fluids with smoothed particle hydrodynamics, *Int. J. Numer. Methods Fluids* 82 (2016) 730–747, <https://doi.org/10.1002/fld.4238>.
- [81] G. Oger, M. Doring, B. Alessandrini, P. Ferrant, An improved SPH method: towards higher order convergence, *J. Comput. Phys.* 225 (2007) 1472–1492, <https://doi.org/10.1016/j.jcp.2007.01.039>.
- [82] P.W. Randles, L.D. Libersky, Smoothed particle hydrodynamics: some recent improvements and applications, *Comput. Methods Appl. Mech. Eng.* 139 (1996) 375–408, [https://doi.org/10.1016/S0045-7825\(96\)01090-0](https://doi.org/10.1016/S0045-7825(96)01090-0).
- [83] J.J. Monaghan, Extrapolating B splines for interpolation, *J. Comput. Phys.* 60 (1985) 253–262, [https://doi.org/10.1016/0021-9991\(85\)90006-3](https://doi.org/10.1016/0021-9991(85)90006-3).
- [84] S. Kularathna, W. Liang, T. Zhao, B. Chandra, J. Zhao, K. Soga, A semi-implicit material point method based on fractional-step method for saturated soil, *Int. J. Numer. Anal. Methods Geomech.* 45 (2021) 1405–1436, <https://doi.org/10.1002/nag.3207>.
- [85] O.C. Zienkiewicz, A.H.C. Chan, M. Pastor, B.A. Schrefler, T. Shiomi, *Computational Geomechanics*, Wiley, Chichester, 1999, [https://doi.org/10.1016/0148-9062\(96\)84010-1](https://doi.org/10.1016/0148-9062(96)84010-1).
- [86] Y.T. Gu, G.R. Liu, Meshless techniques for convection dominated problems, *Comput. Mech.* 38 (2006) 171–182, <https://doi.org/10.1007/s00466-005-0736-8>.
- [87] J. Yang, Z. Yin, F. Laouafa, P. Hicher, Three-dimensional hydromechanical modeling of internal erosion in dike-on-foundation, *Int. J. Numer. Anal. Methods Geomech.* 44 (2020) 1200–1218, <https://doi.org/10.1002/nag.3057>.
- [88] J. Peraire, K. Morgan, O.C. Zienkiewicz, Convection dominated problems, *Am. Soc. Mech. Eng. Appl. Mech. Div. AMD* 78 (1986) 129–147, <https://doi.org/10.1007/1-84628-205-5.5>.
- [89] M. Antuono, A. Colagrossi, S. Marrone, D. Molteni, Free-surface flows solved by means of SPH schemes with numerical diffusive terms, *Comput. Phys. Commun.* 181 (2010) 532–549, <https://doi.org/10.1016/j.cpc.2009.11.002>.
- [90] S. Marrone, A. Colagrossi, D. Le Touzé, G. Graziani, Fast free-surface detection and level-set function definition in SPH solvers, *J. Comput. Phys.* 229 (2010) 3652–3663, <https://doi.org/10.1016/j.jcp.2010.01.019>.
- [91] M.T.V. Genuchten, W.J. Alves, Analytical solutions of the one-dimensional convective-dispersive solute transport equation, (1982). <https://handle.nal.usda.gov/10113/CAT82780278>.
- [92] B.L. Aboustit, S.H. Advani, J.K. Lee, Variational principles and finite element simulations for thermo-elastic consolidation, *Int. J. Numer. Anal. Methods Geomech.* 9 (1985) 49–69, <https://doi.org/10.1002/nag.1610090105>.
- [93] Q. Gao, A. Ghassemi, Three-dimensional thermo-poroelastic modeling and analysis of flow, heat transport and deformation in fractured rock with applications to a lab-scale geothermal system, *Rock Mech. Rock Eng.* 53 (2020) 1565–1586, <https://doi.org/10.1007/s00603-019-01989-0>.
- [94] P. Delage, On the thermal impact on the excavation damaged zone around deep radioactive waste disposal, *J. Rock Mech. Geotech. Eng.* 5 (2013) 179–190, <https://doi.org/10.1016/j.jrmge.2013.04.002>.